ARTICLE

Reversible Mn²⁺/Mn⁴⁺ double redox in lithium–excess cathode materials

Jinhyuk Lee[1,9]*, Daniil A. Kitchaev[2], Deok-Hwang Kwon[1], Chang-Wook Lee[3], Joseph K. Papp[4], Yi-Sheng Liu[5], Zhengyan Lun[1], Raphaële J. Clément[1], Tan Shi[1], Bryan D. McCloskey[4,6], Jinghua Guo[5,7], Mahalingam Balasubramanian[3] & Gerbrand Ceder[1,8]*

There is an urgent need for low-cost, resource-friendly, high-energy-density cathode materials for lithium-ion batteries to satisfy the rapidly increasing need for electrical energy storage. To replace the nickel and cobalt, which are limited resources and are associated with safety problems, in current lithium-ion batteries, high-capacity cathodes based on manganese would be particularly desirable owing to the low cost and high abundance of the metal, and the intrinsic stability of the Mn⁴⁺ oxidation state. Here we present a strategy of combining high-valent cations and the partial substitution of fluorine for oxygen in a disordered-rocksalt structure to incorporate the reversible Mn²⁺/Mn⁴⁺ double redox couple into lithium-excess cathode materials. The lithium-rich cathodes thus produced have high capacity and energy density. The use of the Mn²⁺/Mn⁴⁺ redox reduces oxygen redox activity, thereby stabilizing the materials, and opens up new opportunities for the design of high-performance manganese-rich cathodes for advanced lithium-ion batteries.

Lithium-ion-based energy storage is becoming a pervasive technology in today's society. Introduced in the early 1990s for use in portable electronics, it has now migrated to applications such as transportation and grid, for which energy storage needs will soon dwarf the use in electronics[1,2]. Indeed, today, with electric vehicles making up about 1% of all car sales, almost half of all Li-ion batteries produced are already directed towards transportation. These new applications increase the demand for safe high-energy storage at low cost and without relying on constrained natural resources[1,2]. In this context, it is remarkable that almost all Li-ion cathode materials rely on only two transition metals, Ni and Co, which are the electroactive elements in the layered-rocksalt cathode materials in the $Li(Ni,Mn,Co)O_2$ chemical space (NMCs)[3]. On one end of this compositional spectrum, $LiCoO_2$ dominates the electronics sector, whereas Ni-rich materials are of interest for the automotive sector[2]. Although Mn has been used in a spinel cathode[4], and Fe in the $LiFePO_4$ olivine[5], these compounds suffer from low energy density. Given the limits of energy density that can be achieved with the layered NMCs and the potential resource constraints on cobalt[2], it is of interest to develop high-capacity cathode materials based on other redox metals. In particular, transition metals that can exchange two electrons are of interest for their ability to create high capacity, similar to the Ni^{2+}/Ni^{4+} couple in NMC cathodes. Low cost and low toxicity make the Mn^{2+}/Mn^{4+} couple particularly desirable[6] for designing high-performance Li-ion batteries that are also inexpensive and eco-friendly.

Manganese is currently used in cathode materials, but mostly in the inert Mn^{4+} state, as in NMC cathodes, or for its Mn^{3+}/Mn^{4+} couple, as in $LiMn_2O_4$ spinel[1,3,4,7]. More recently, Mn^{3+} has been used in disordered-rocksalt-type cathodes, such as $Li_{1.3}Mn_{0.4}Nb_{0.3}O_2$, in which the low capacity from Mn^{3+}/Mn^{4+} needs to be overcome by a large amount of oxygen redox[8], which can trigger O loss, resulting in substantial voltage and capacity fade[7,9,10]. In $Li_4Mn_2O_5$, a high initial capacity (>300 mAh g⁻¹) is achieved by oxidizing Mn^{3+} past the

standard Mn^{3+}/Mn^{4+} redox couple, but this causes substantial voltage and capacity fade in subsequent cycles[11]. In our approach, we start instead from Mn^{2+} in the discharged state so that a high theoretical capacity can be obtained by oxidizing to Mn^{4+} without relying on O redox. Cycling between two stable valence states of Mn, and limiting the O redox, is expected to improve the reversibility of the charge/discharge process. Reduction to Mn^{2+} has been observed[12] by lithiation of amorphous $Li_{1.5}Na_{0.5}MnO_{2.85}I_{0.12}$, but as this cathode material is synthesized in the charged state it does not enable Li to be brought into the Li-ion cell. The development of a high-performance Li-ion cathode based on the Mn^{2+}/Mn^{4+} couple requires a material that forms in its discharged state, contains enough Mn^{2+} and Li^+ ions to provide high capacity and preferably crystallizes in a dense structure, such as the layered or disordered-rocksalt structure, to maximize its volumetric energy density. Introducing Mn^{2+} in the dense layered or disordered materials has been difficult, as the Li excess ($x > 1$ in $Li_xTM_{2-x}O_2$, where TM is transition metal) required to achieve high practical capacity[10,13,14] demands a high average transition metal valence.

In this work, we demonstrate that high capacity (>300 mAh g⁻¹) and energy density (about 1,000 Wh kg⁻¹) can be achieved in disordered-rocksalt Li-rich intercalation cathodes from Mn^{2+}/Mn^{4+} double redox combined with a small amount of O redox. A critical step is that we are able to lower the Mn valence in the cathode material through a combined strategy of high-valent cation (Nb^{5+}, Ti^{4+}) substitution[8] and O^{2-} replacement[15–17] by F⁻. This O^{2-} replacement was recently shown to be aided by Li excess and cation disorder[15]. We target the Mn^{2+}-containing compositions $Li_2Mn_{2/3}Nb_{1/3}O_2F$ and $Li_2Mn_{1/2}Ti_{1/2}O_2F$, which have a theoretical Mn^{2+}/Mn^{4+} redox capacity of 270 mAh g⁻¹ and 230 mAh g⁻¹, respectively. Given the high Mn capacities, only a small amount of O redox is required for these materials to deliver a total capacity over 300 mAh g⁻¹, mitigating problems related to O redox. Thus realized, high capacity from Mn^{2+}/Mn^{4+} double redox

---

[1]Department of Materials Science and Engineering, University of California, Berkeley, CA, USA. [2]Department of Materials Science and Engineering, Massachusetts Institute of Technology, Cambridge, MA, USA. [3]X-ray Science Division, Advanced Photon Source, Argonne National Laboratory, Argonne, IL, USA. [4]Department of Chemical and Biomolecular Engineering, University of California, Berkeley, CA, USA. [5]Advanced Light Source, Lawrence Berkeley National Laboratory, Berkeley, CA, USA. [6]Energy Storage and Distributed Resources Division, Lawrence Berkeley National Laboratory, Berkeley, CA, USA. [7]Department of Chemistry and Biochemistry, University of California, Santa Cruz, CA, USA. [8]Materials Science Division, Lawrence Berkeley National Laboratory, Berkeley, CA, USA. [9]Present address: Department of Nuclear Science and Engineering, Massachusetts Institute of Technology, Cambridge, MA, USA. *e-mail: jinhyuk@mit.edu; gceder@berkeley.edu
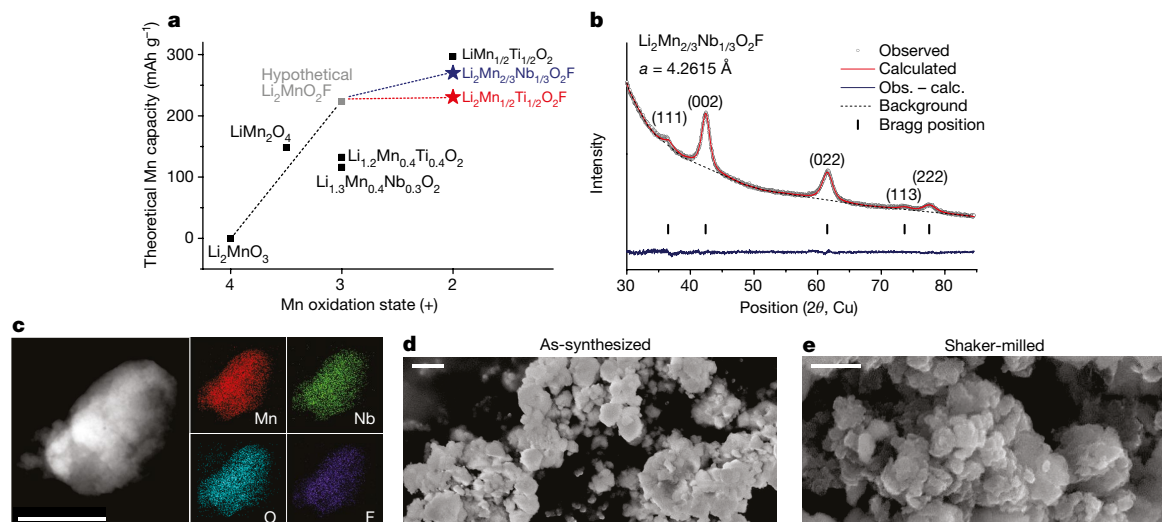
Fig. 1 | Design and structural characterization of Li₂Mn₂/₃Nb₁/₃O₂F. a, Theoretical Mn-redox capacity of various Mn-based cathode materials. b, The X-ray diffraction pattern of $Li_2Mn_{2/3}Nb_{1/3}O_2F$. c, EDS mapping (Mn, Nb, O, F) on a $Li_2Mn_{2/3}Nb_{1/3}O_2F$ particle. Scale bar, 100 nm. d, e, SEM images of $Li_2Mn_{2/3}Nb_{1/3}O_2F$: d, as-synthesized (scale bar, 400 nm) and e, shaker-milled with carbon black (scale bar, 200 nm).

opens new opportunities for the design of high-performance Li-ion cathode materials.

Structural characterization of Li₂Mn₂/₃Nb₁/₃O₂F

To evaluate the Mn^{2+}/Mn^{4+} redox strategy, we first test a new disordered Li-rich material: $Li_2Mn_{2/3}Nb_{1/3}O_2F$ (equivalent to $Li_{1.333}Mn_{0.444}Nb_{0.222}O_{1.333}F_{0.667}$), synthesized by a mechanochemical ball-milling method[11,16,17]. The combined presence of high-valent Nb^{5+} and low-valent F^- sets up the charge balance to incorporate Mn as Mn^{2+} in the pristine $Li_2Mn_{2/3}Nb_{1/3}O_2F$ material, leading to a very high theoretical Mn-redox capacity of 270 mAh g⁻¹, which is more than twice that of a typical Mn-based Li-rich cathode material (Fig. 1a). In addition, the d^0 configuration of Nb^{5+} (similar to that of Ti^{4+}, V^{5+}, Zr^{4+} and Mo^{6+}) promotes the formation of a disordered-rocksalt structure[18].

X-ray diffraction (XRD) patterns (Fig. 1b, Extended Data Table 1) and elemental analysis (Extended Data Table 2) show that the compound forms in a disordered-rocksalt phase with a composition close to the target composition[11]. XRD refinement yields a lattice parameter of about 4.262 Å (Extended Data Table 1). Energy-dispersive spectroscopy mapping (EDS) on a $Li_2Mn_{2/3}Nb_{1/3}O_2F$ particle, using a transmission electron microscope (TEM), reveals a uniform distribution of Mn, Nb, O and F (Fig. 1c). Results of ^7Li and ^{19}F nuclear magnetic resonance (NMR) reveal that some Li can be found in diamagnetic environments and some F can be found in LiF-like environments (Extended Data Fig. 1, Methods section 'Supplementary Note 1'). Although this suggests that small amounts of impurity phases (for example LiF, Li_2O, Li_2CO_3) may be present in the as-synthesized $Li_2Mn_{2/3}Nb_{1/3}O_2F$ sample, we cannot rule out the presence of diamagnetic or LiF-like local domains in the rocksalt phase. In fact, no crystalline impurities could be detected with XRD. TEM shows that the primary particles are polycrystalline and made of crystalline grains about 15 nm in size (Extended Data Fig. 2). No amorphous components were detected in TEM, indicating that the electrochemical properties are predominantly determined by the $Li_2Mn_{2/3}Nb_{1/3}O_2F$ phase. Scanning electron microscopy (SEM) shows that the primary particle size of the as-prepared $Li_2Mn_{2/3}Nb_{1/3}O_2F$ compound is 100–300 nm (Fig. 1d), which is reduced to less than 100 nm after mixing with carbon black using a shaker-mill for electrode fabrication (Fig. 1e).

Electrochemical performance of Li₂Mn₂/₃Nb₁/₃O₂F

Galvanostatic charge–discharge tests of $Li_2Mn_{2/3}Nb_{1/3}O_2F$ at 20 mA g⁻¹ show a discharge capacity of 238 mAh g⁻¹ (708 Wh kg⁻¹) between 1.5 V and 4.6 V, which increases to 277 mAh g⁻¹ (849 Wh kg⁻¹) and 304 mAh g⁻¹ (945 Wh kg⁻¹) with higher charge cut-off voltages of

4.8 V and 5.0 V, respectively (Fig. 2a–c). In a test between 1.5 V and 5.0 V at 10 mA g⁻¹ (Fig. 2d), the discharge capacity further increases to 317 mAh g⁻¹, delivering a very high energy content of 995 Wh kg⁻¹ (3,761 Wh l⁻¹). This discharge capacity of about 320 mAh g⁻¹ and specific energy approaching 1,000 Wh kg⁻¹ are among the highest values achieved by Li-ion intercalation cathodes[10–12,19]. The reversible capacity and energy density at 20 mA g⁻¹ decrease to 233 mAh g⁻¹ (180 mAh g⁻¹) and 760 Wh kg⁻¹ (600 Wh kg⁻¹), respectively, as the voltage window is reduced to 2.0–4.8 V (2.3–4.6 V) (Extended Data Fig. 3). The rate capability of $Li_2Mn_{2/3}Nb_{1/3}O_2F$ is fairly good. Figure 2e compares the first cycle profiles of $Li_2Mn_{2/3}Nb_{1/3}O_2F$ under different rates between 1.5 V and 5.0 V. The material delivers as high as 226 mAh g⁻¹ (695 Wh kg⁻¹) at 200 mA g⁻¹ and up to 140 mAh g⁻¹ (410 Wh kg⁻¹) at a very high rate of 1,000 mA g⁻¹ (Extended Data Fig. 4). The data presented here were obtained on electrode films made of 60 wt% active material, but the performance is similar for electrodes with a higher loading of 70 wt% and 80 wt% (Extended Data Fig. 3).

The voltage profiles of $Li_2Mn_{2/3}Nb_{1/3}O_2F$ do not contain significant hysteresis and remain nearly identical during cycling, suggesting that structural changes and oxygen loss are small[8,20,21]. Only upon very high-voltage charging to above 4.7 V is an apparent voltage plateau observed which is barely seen in discharge (Fig. 2f). As $Li_2Mn_{2/3}Nb_{1/3}O_2F$ delivers a higher capacity than its theoretical Mn capacity (270 mAh g⁻¹), we expect that the charge plateau at about 4.8 V accompanies O-oxidation. The asymmetry in charge/discharge voltage is similar to previous observations in which the O-oxidation plateau is not recovered in the discharge[8,20,21]. Nevertheless, this plateau in $Li_2Mn_{2/3}Nb_{1/3}O_2F$ appears only after charging above about 250 mAh g⁻¹, leading to less voltage hysteresis than for the other Mn-redox-active disordered compounds in which the O-oxidation plateau occurs typically much earlier in the charge[8,20,21]. The smaller amount of O-oxidation and negligible changes in the voltage profile of $Li_2Mn_{2/3}Nb_{1/3}O_2F$ are further supported by differential electrochemical mass spectrometry (DEMS) results, which show negligible O_2 (g) evolution up to a charge of 5 V (Extended Data Fig. 5, Methods section 'Supplementary Note 2'). In addition, voltage fade is small in this material (Extended Data Fig. 6, Methods section 'Supplementary Note 3'). These results indicate that our strategy of going to Mn^{2+} compounds to increase the Mn-redox capacity at the expense of O redox is successful in increasing capacity and reversibility.

Redox mechanism of Li₂Mn₂/₃Nb₁/₃O₂F

The redox mechanism and structural evolution of $Li_2Mn_{2/3}Nb_{1/3}O_2F$ have been further studied by X-ray diffraction, and by hard X-ray and
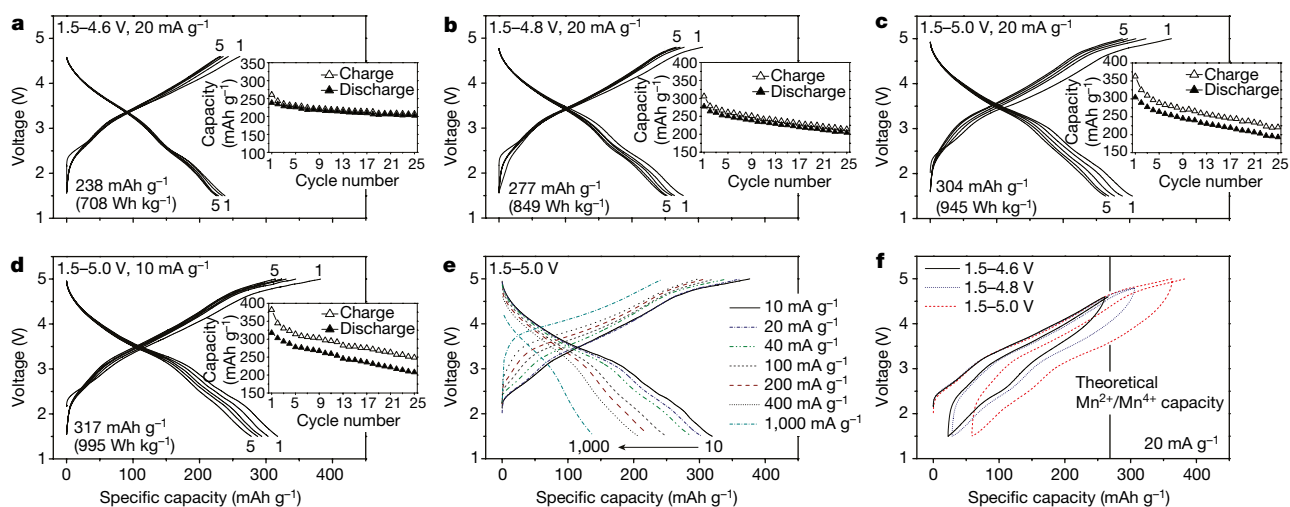
Fig. 2 | Electrochemical performance of Li₂Mn₂/₃Nb₁/₃O₂F. a–d, Voltage profiles and capacity retention of $Li_2Mn_{2/3}Nb_{1/3}O_2F$ under various cycling conditions: **a**, 1.5–4.6 V, 20 mA g^{-1}; **b**, 1.5–4.8 V, 20 mA g^{-1}; **c**, 1.5–5.0 V, 20 mA g^{-1}; and **d**, 1.5–5.0 V, 10 mA g^{-1}. **e**, The first-cycle voltage profiles of $Li_2Mn_{2/3}Nb_{1/3}O_2F$ when cycled between 1.5 V and 5.0 V at 10, 20, 40, 100, 200, 400 and 1,000 mA g^{-1}. **f**, The first-cycle and second-charge profiles of $Li_2Mn_{2/3}Nb_{1/3}O_2F$ under different voltage windows: 1.5–4.6 V, 1.5–4.8 V and 1.5–5.0 V. All tests were conducted at room temperature.

soft X-ray absorption spectroscopies. Figure 3a shows a reversible lattice-parameter change upon cycling, as observed in other disordered-rocksalt intercalation cathodes[8,20–22]. The shift of the (002) and (022) peaks to a higher angle upon charge (indicating a decrease of lattice parameters) is recovered on discharge. Upon charging, the *a* lattice parameter decreases from 4.258 Å to 4.130 Å at the top of charge and returns to 4.250 Å after full discharge.

Hard X-ray absorption spectroscopy (XAS) suggests that Mn^{2+} is oxidized during charge towards Mn^{4+}, a process that is reversed upon discharge. Figure 3b shows the Mn K-edge X-ray absorption near-edge structure (XANES) for $Li_2Mn_{2/3}Nb_{1/3}O_2F$ at various states of charge and discharge. As the charge capacity increases from 0 to 135 mA h g^{-1} and 270 mAh g^{-1}, the Mn K-edge shifts from an energy close to MnO (Mn^{2+} reference) to that of Mn₂O₃ (Mn^{3+} reference) and then partway to the energy seen in MnO₂ (Mn^{4+} reference). Further charging to 360 mAh g^{-1} leads to only minor shifts. The Mn K-edge almost completely returns to its original position after discharge. Although the exact amount of each valence state cannot be quantified, as the near-edge structure is sensitive to both the oxidation state and bonding environment[23], this result suggests that, on full charge, Mn^{2+} is oxidized to Mn^{4+} with some Mn^{2+} or Mn^{3+} ions remaining. Full recovery to Mn^{2+} occurs on discharge. This interpretation is further supported by a derivative analysis on the Mn pre-edge at about 6,540 eV (Extended Data Fig. 7, Methods section

'Supplementary Note 4'). The species Nb^{5+} does not participate in redox processes (Extended Data Fig. 8).

Whereas hard X-rays probe metal oxidation, soft X-ray absorption using a total fluorescence yield can be used to investigate oxygen redox behaviour. Figure 3c traces the pre-edge features of the O K-edge XAS spectra of $Li_2Mn_{2/3}Nb_{1/3}O_2F$ at various states of charge. The pre-edge is primarily associated with the O 1*s* to 2*p* transition, and its intensity is attributable to the density of unoccupied Nb 4*d*–O 2*p* and Mn 3*d*–O 2*p* hybridized states. We associate the pre-edge feature around 530.9 eV with unoccupied Nb 4*d*–O 2*p* hybridized states, as Mn^{2+} oxides (for example MnO) typically exhibit a pre-edge feature above[24,25] about 533 eV. Charging to 135 mAh g^{-1} (theoretical Mn^{2+}/Mn^{3+} limit) increases the intensity in the 529–532 eV range which is typical for Mn^{3+} oxides such as[21,25] Mn₂O₃. After charging to 270 mAh g^{-1} and 360 mAh g^{-1}, an intensity gain is observed broadly between 528 and 530 eV. The largest major intensity gain is centred around 529 eV (feature A) which is characteristic of Mn^{4+} oxides (for example MnO₂, Li₂MnO₃)[24–26], suggesting some Mn^{3+}/Mn^{4+} oxidation on charge. Along with this feature A, we see an intensity gain at 530–531 eV (feature B) after charging to 270 mAh g^{-1} and 360 mAh g^{-1}. Previously, O oxidation has been shown to create a broad component around 530.2 eV in Mn-based disordered Li-rich cathodes[8,21]. Therefore, this feature B most probably indicates O oxidation which concurrently occurs with Mn^{3+}/Mn^{4+} oxidation. Discharging to 320 mAh g^{-1} restores the
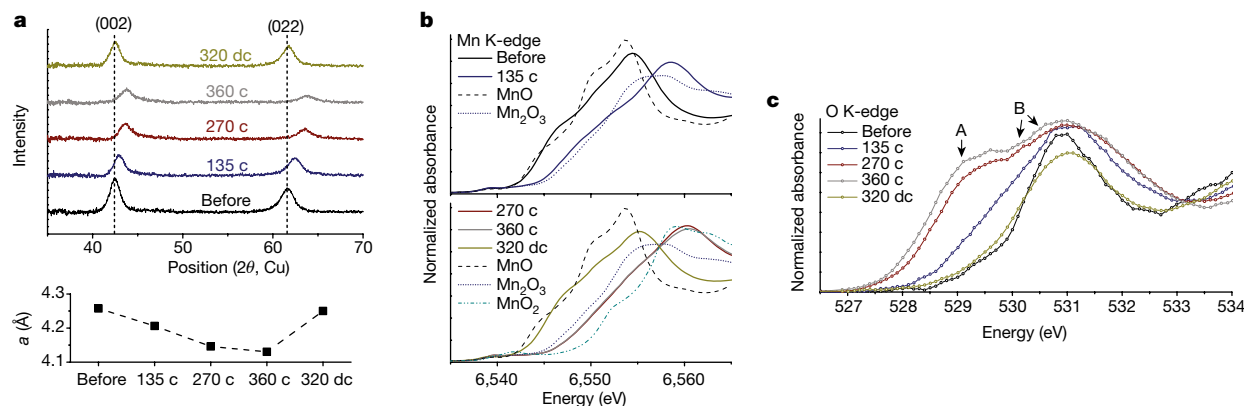

Fig. 3 | Reaction mechanism of Li₂Mn₂/₃Nb₁/₃O₂F. a, XRD patterns of $Li_2Mn_{2/3}Nb_{1/3}O_2F$ during the first cycle at 10 mA g^{-1} and the refined *a*-lattice parameters (c, charge; dc, discharge). **b, c**, Manganese K-edge XANES spectra from hard XAS (**b**) and O K-edge spectra from soft XAS (**c**; using total fluorescence yield mode) during the initial cycle. Features A and B are described in the text. Plots are shown for $Li_2Mn_{2/3}Nb_{1/3}O_2F$ before cycling; 135 mAh g^{-1} charged; 270 mAh g^{-1} charged; 360 mAh g^{-1} charged; 320 mAh g^{-1} discharged after a 375 mAh g^{-1} charge.
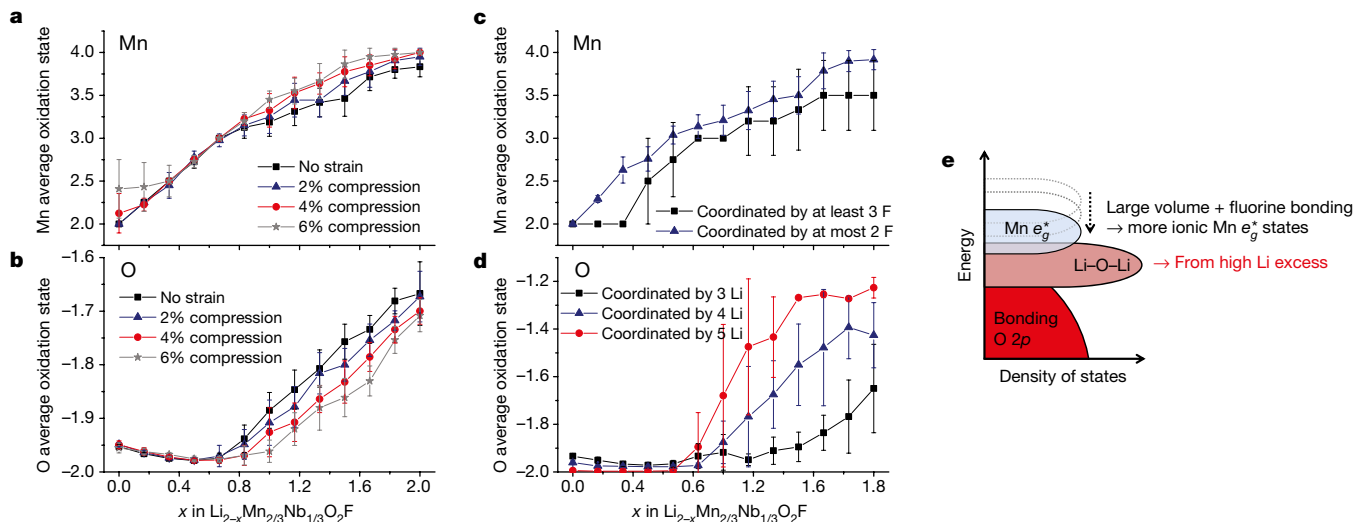
Fig. 4 | Ab initio calculations of the redox mechanism of Li₂Mn₂/₃Nb₁/₃O₂F. a, b, Manganese (**a**) and oxygen (**b**) average oxidation state as a function of delithiation (x in $Li_{2-x}Mn_{2/3}Nb_{1/3}O_2F$) and artificially introduced strain relative to the discharged state ($x = 0$). **c**, Change in the average oxidation state of Mn atoms that are coordinated by three or more fluorine atoms and those coordinated by two or fewer fluorine atoms. **d**, Change in the average oxidation state of O atoms with three, four and five Li nearest neighbours in the fully lithiated state ($x = 0$). The data in **c** and **d** were collected from model structures without strain and are representative of trends seen at all levels of strain. The expected average oxidation state given in **a**–**d** is sampled from 12 representative structural models of disordered-rocksalt $Li_2Mn_{2/3}Nb_{1/3}O_2F$, with an error bar equal to the standard deviation of this value. **e**, A schematic band structure of $Li_2Mn_{2/3}Nb_{1/3}O_2F$.

pre-edge shape and intensity, indicating Mn and O reduction. Hence, the electrochemical processes in this compound are reversible.

Ab initio study of Li₂Mn₂/₃Nb₁/₃O₂F

In conventional Li–Mn oxides (for example LiMnO₂, Li₂MnO₃), Mn oxidation up to Mn⁴⁺ is not competitive with O oxidation[8,10,20,21]. The question is then why there is a partial overlap between these redox processes in $Li_2Mn_{2/3}Nb_{1/3}O_2F$. The main differences between $Li_2Mn_{2/3}Nb_{1/3}O_2F$ and other Mn-based Li-excess oxides are the presence of fluorine and the relatively large lattice parameter (a is about 4.26 Å for $Li_2Mn_{2/3}Nb_{1/3}O_2F$ compared with about 4.19 Å for $Li_{1.3}Mn_{0.4}Nb_{0.3}O_2$)[8,20,21] which leads to a larger distance between Mn and the ligand. To elucidate the impact of these features on electrochemical behaviour, we study the effect of F-coordination and lattice volume on the redox mechanism using density functional theory calculations. Note that although we compute the redox mechanism through electron titration as described in the Methods section, for clarity we refer to the degree of charge in terms of Li content.

Figure 4a, b shows the Mn and O average oxidation states as a function of delithiation (x in $Li_{2-x}Mn_{2/3}Nb_{1/3}O_2F$) and for varying degrees of compressive strain relative to the fully relaxed discharged state (($l_0 - l)/l_0 \times 100\%$, where l_0 is the lattice parameter of the fully relaxed discharged state and l is the compressed lattice parameter). The vertical bars account for the range of results obtained from various structural models of disordered-rocksalt $Li_2Mn_{2/3}Nb_{1/3}O_2F$. Initial delithiation up to $x = 0.667$ (theoretical Mn²⁺/Mn³⁺ limit) modifies only the Mn oxidation state, but further Li removal leads to concurrent O and Mn oxidation. Smaller lattice volume increases the degree of Mn³⁺/Mn⁴⁺ oxidation at a fixed lithium level. At 270 mAh g⁻¹ charge ($x = 1.333$), the experimentally observed lattice parameter reduction is 2.6% (Fig. 3a). At this strain, the calculations indicate average oxidation states of approximately Mn³·⁵⁺ and O¹·⁸⁻, supporting the presence of an overlap between Mn³⁺/Mn⁴⁺ and O redox, and fully consistent with our experimental results. This result seems to indicate that the large lattice parameter of $Li_2Mn_{2/3}Nb_{1/3}O_2F$ is partly responsible for the overlap.

Figure 4c,d clarifies the impact of local environment on the oxidation of Mn and O. Figure 4c compares the average oxidation state of Mn atoms that have two or fewer F ligands out of six anion neighbours with that of Mn with three or more F ligands. At a given level

of delithiation, Mn atoms with high F-coordination are less oxidized than those with low F-coordination, indicating that the substitution of O by F favours lower Mn oxidation states and thus leads to more redox overlap with oxygen. On the oxygen side, we observe more oxidation from O atoms with five and four Li nearest neighbours than those with three Li neighbours (Fig. 4d). This trend is consistent with previous theory and experiments that indicate that the lack of transition-metal–O hybridization in Li-rich environments increases the energy of some oxygen orbitals so that they can be more easily oxidized[26–28]. Hence, the presence of Mn–F bonds, the Li-excess O environments and the larger bond distance of Mn–O(F) in this material all contribute to some competitive Mn/O oxidation at very high states of charge (Fig. 4e). Nevertheless, owing to the large Mn²⁺/Mn⁴⁺ reservoir, O redox is much less needed in $Li_2Mn_{2/3}Nb_{1/3}O_2F$ than in other Mn-based Li-rich materials, rendering Mn double redox an effective way to achieve high capacity without the typical polarization and capacity fade that is observed with excessive use of the oxygen redox.

Structure and performance of Li₂Mn₁/₂Ti₁/₂O₂F

With diverse choices of high valent cations, Mn²⁺/Mn⁴⁺ double redox can be realized in many different systems. As a demonstration, we have developed another new material, $Li_2Mn_{1/2}Ti_{1/2}O_2F$, in which Ti⁴⁺ is the high-valent cationic species. This material also forms a disordered-rocksalt phase ($a = 4.206$ Å), as can be inferred from the XRD pattern in Fig. 5a (Extended Data Table 1). SEM shows that, after mixing the compound with carbon black using a shaker-mill, the average primary particle size is about 50 nm (Fig. 5b). TEM-EDS shows a uniform distribution of Mn, Ti, O and F (Fig. 5c). As in the case of $Li_2Mn_{2/3}Nb_{1/3}O_2F$, the primary particles of $Li_2Mn_{1/2}Ti_{1/2}O_2F$ are polycrystalline and made of grains about 15 nm across (Extended Data Fig. 9). The ⁷Li and ¹⁹F NMR results suggest the possible presence of impurities (for example LiF, Li₂O, Li₂CO₃) in our sample (Extended Data Fig. 1), but their amount is likely to be small as no crystalline or amorphous impurities could be observed with XRD and TEM (Fig. 5a, Extended Data Fig. 9).

$Li_2Mn_{1/2}Ti_{1/2}O_2F$ delivers high capacities similar to $Li_2Mn_{2/3}Nb_{1/3}O_2F$. When cycled between 1.6 V and 4.8 V (Fig. 5d) or 1.5 V and 5.0 V (Fig. 5e) at 20 mA g⁻¹, this material yields reversible capacities of 259 mAh g⁻¹ (783 Wh kg⁻¹, 2,756 Wh l⁻¹) and 321 mAh g⁻¹ (932 Wh kg⁻¹, 3,281 Wh l⁻¹), respectively. These values are again

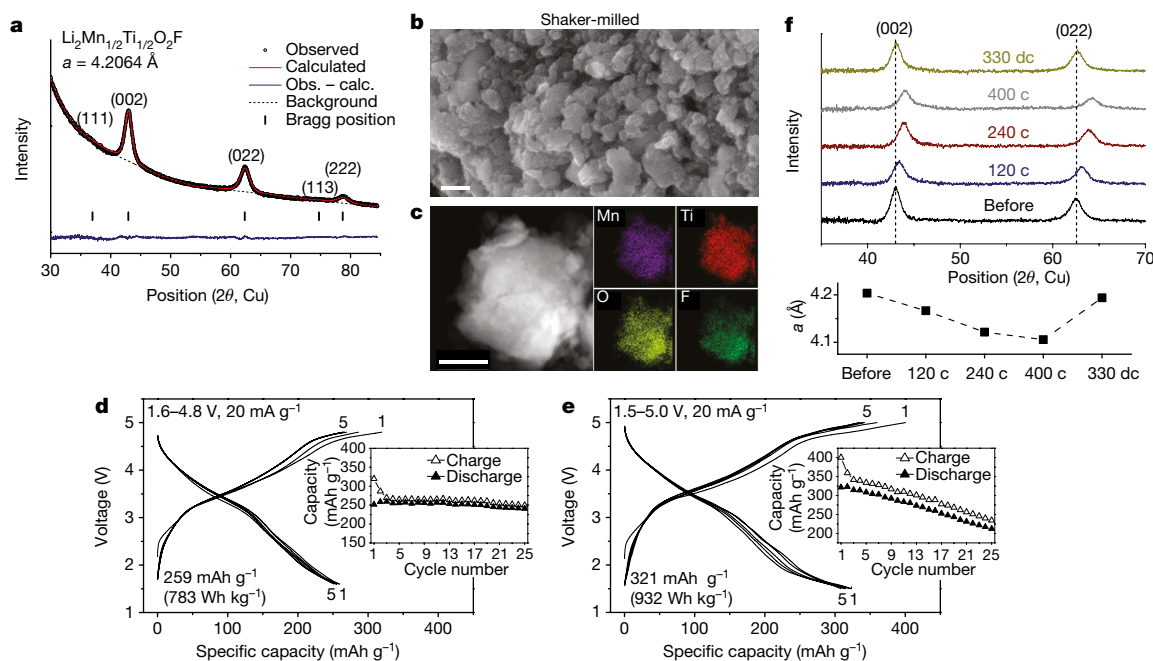**Fig. 5 | Structural characterization and electrochemical performance of $Li_2Mn_{1/2}Ti_{1/2}O_2F$. a**, The XRD pattern of $Li_2Mn_{1/2}Ti_{1/2}O_2F$. **b**, SEM image of $Li_2Mn_{1/2}Ti_{1/2}O_2F$ after shaker-milling with carbon black for electrode fabrication. Scale bar, 100 nm. **c**, EDS mapping (Mn, Ti, O, F) on a $Li_2Mn_{1/2}Ti_{1/2}O_2F$ particle. Scale bar, 200 nm. **d**, **e**, Voltage profiles and capacity retention of $Li_2Mn_{1/2}Ti_{1/2}O_2F$ when cycled at 20 mA g^{-1} between 1.6 V and 4.8 V (**d**), and 1.5 V and 5.0 V (**e**). Cycling tests were conducted at room temperature. **f**, The XRD patterns of $Li_2Mn_{1/2}Ti_{1/2}O_2F$ during the first cycle at 10 mA g^{-1} and the refined *a*-lattice parameters: before cycling; 120 mAh g^{-1} charged; 240 mAh g^{-1} charged; 400 mAh g^{-1} charged; 330 mAh g^{-1} discharged after a 400 mAh g^{-1} charge.

among the highest values achieved by advanced cathode materials[10,19]. Additional electrochemical data (rate tests, voltage window tests, change of the electrode formulation) are presented and discussed in Extended Data Fig. 10 and Methods section 'Supplementary Note 5'.

As in $Li_2Mn_{2/3}Nb_{1/3}O_2F$, the voltage profiles of $Li_2Mn_{1/2}Ti_{1/2}O_2F$ barely change after the first cycle, indicating a reversible reaction without a major structural change or O loss, as evidenced by the DEMS results (Extended Data Fig. 5). The O-oxidation plateau appears only after charging above 230 mAh g^{-1} (above about 4.6 V), which is substantially delayed compared with other Mn-based Li-rich materials. Nevertheless, this plateau is slightly longer than in $Li_2Mn_{2/3}Nb_{1/3}O_2F$, probably owing to the smaller Mn^{2+} content in $Li_2Mn_{1/2}Ti_{1/2}O_2F$, requiring more O oxidation to achieve a given capacity.

Ex situ XRD of $Li_2Mn_{1/2}Ti_{1/2}O_2F$ indicates a reversible change in lattice parameter, shrinking from about 4.203 Å to about 4.105 Å after a 400 mAh g^{-1} charge and then recovering to about 4.194 Å after a 330 mAh g^{-1} discharge (Fig. 5f). Hard XAS confirms Mn^{2+}/Mn^{4+} redox in the material (Extended Data Fig. 11, Methods section 'Supplementary Note 6'). As in $Li_2Mn_{2/3}Nb_{1/3}O_2F$, additional capacity beyond Mn-redox capacity is probably delivered by O redox. Based on its high capacity and reversibility, $Li_2Mn_{1/2}Ti_{1/2}O_2F$ has considerable potential as a high-performance Li-ion cathode.

Outlook for Mn^{2+}/Mn^{4+} redox

Double redox couples are tremendously important for the development of advanced cathodes. Indeed, today's modern NMC-based layered cathodes all rely to some extent on the Ni^{2+}/Ni^{4+} double redox. With $Li_2Mn_{2/3}Nb_{1/3}O_2F$ and $Li_2Mn_{1/2}Ti_{1/2}O_2F$, we have demonstrated that combined fluorination and high-valent cation substitution can introduce Mn^{2+}/Mn^{4+} redox in a Li-excess disordered-rocksalt structure, which leads to high-capacity Mn-based Li-excess cathodes (capacity of >300 mAh g^{-1}, energy density of around 1,000 Wh kg^{-1}) without an excessive use of O redox. This discovery is important, as our strategy can be widely applied to design high-performance Mn-based Li-excess cathodes that do not suffer from structural degradation triggered by extensive O redox.

The combination of Mn^{2+}/Mn^{4+} redox with the cation-disordered structure[8,13,20,22] and the partial replacement of O by F[15–17,29] leads to a large chemical space for new cathode materials. We expect to see considerable optimization through the use of different high-valent charge-compensating elements, as well as through minor alloying additions to stabilize the structure further and increase other performance aspects. The disordered-rocksalt framework has previously shown high structural stability[8,11,13,20–22], and its compositional flexibility, enabled by not requiring the preservation of the layered cathode structure, can be used to tune not only the Li-excess level for Li transport[13,14], but also the content of F and high-valent cations (such as Sn^{4+}, Sb^{5+} and Te^{6+}). These handles can all be used to modify the size of the Mn^{2+}/Mn^{4+} reservoir and balance Mn- and O-redox activities. Critical directions for further research include finding ways of decreasing the voltage slope of these compounds, so that their high capacity and energy density can be delivered over a narrower voltage window[30], as well as investigating Mn dissolution which often undermines the long-term cyclability of Mn-based cathodes[31]. Strategies based on compositional modifications of the cathode material, on changes in the short-range cation distribution, on microstructure control (for example by surface coating)[31] and on the use of tailored electrolytes[32,33] should be explored to further develop high-performance Mn^{2+}/Mn^{4+}-based cathodes for advanced Li-ion batteries.

Online content

Any Methods, including any statements of data availability and Nature Research reporting summaries, along with any additional references and Source Data files, are available in the online version of the paper at https://doi.org/10.1038/s41586-018-0015-4.

1. Whittingham, M. S. Lithium batteries and cathode materials. *Chem. Rev.* **104**, 4271–4302 (2004).
2. Olivetti, E. A., Ceder, G., Gaustad, G. G. & Fu, X. Lithium-ion battery supply chain considerations: analysis of potential bottlenecks in critical metals. *Joule* **1**, 229–243 (2017).

3. Lu, Z., MacNeil, D. D. & Dahn, J. R. Layered Li[Ni$_x$Co$_{1-2x}$Mn$_x$]O$_2$ cathode materials for lithium-ion batteries. *Electrochem. Solid-State Lett* **4**, A200–A203 (2001).
4. Thackeray, M. M., Johnson, P. J., de Picciotto, L. A., Bruce, P. G. & Goodenough, J. B. Electrochemical extraction of lithium from LiMn$_2$O$_4$. *Mater. Res. Bull.* **19**, 179–187 (1984).
5. Kang, B. & Ceder, G. Battery materials for ultrafast charging and discharging. *Nature* **458**, 190–193 (2009).
6. Nitta, N., Wu, F., Lee, J. T. & Yushin, G. Li-ion battery materials: present and future. *Mater. Today* **18**, 252–264 (2015).
7. Thackeray, M. M. et al. Li$_2$MnO$_3$-stabilized LiMO$_2$ (M = Mn, Ni, Co) electrodes for lithium-ion batteries. *J. Mater. Chem.* **17**, 3112–3125 (2007).
8. Yabuuchi, N. et al. High-capacity electrode materials for rechargeable lithium batteries: Li$_3$NbO$_4$-based system with cation-disordered rocksalt structure. *Proc. Natl Acad. Sci. USA* **112**, 7650–7655 (2015).
9. Armstrong, A. R. et al. Demonstrating oxygen loss and associated structural reorganization in the lithium battery cathode Li[Ni$_{0.2}$Li$_{0.2}$Mn$_{0.6}$]O$_2$. *J. Am. Chem. Soc.* **128**, 8694–8698 (2006).
10. Hy, S. et al. Performance and design considerations for lithium excess layered oxide positive electrode materials for lithium ion batteries. *Energy Environ. Sci.* **9**, 1931–1954 (2016).
11. Freire, M. et al. A new active Li–Mn–O compound for high energy density Li-ion batteries. *Nat. Mater.* **15**, 173–177 (2016).
12. Kim, J. & Manthiram, A. A manganese oxyiodide cathode for rechargeable lithium batteries. *Nature* **390**, 265–267 (1997).
13. Lee, J. et al. Unlocking the potential of cation-disordered oxides for rechargeable lithium batteries. *Science* **343**, 519–522 (2014).
14. Urban, A., Lee, J. & Ceder, G. The configurational space of rocksalt-type oxides for high-capacity lithium battery electrodes. *Adv. Energy Mater.* **4**, 1400478 (2014).
15. Richards, W. D., Dacek, S. T., Kitchaev, D. A. & Ceder, G. Fluorination of lithium-excess transition metal oxide cathode materials. *Adv. Energy Mater.* **343**, 1701533 (2017).
16. Chen, R. et al. Disordered lithium-rich oxyfluoride as a stable host for enhanced Li$^+$ intercalation storage. *Adv. Energy Mater.* **5**, 1401814 (2015).
17. Takeda, N. et al. Reversible Li storage for nanosize cation/anion-disordered rocksalt-type oxyfluorides: LiMoO$_{2-x}$ LiF (0≤x≤2) binary system. *J. Power Sources* **367**, 122–129 (2017).
18. Urban, A., Abdellahi, A., Dacek, S., Artrith, N. & Ceder, G. Electronic-structure origin of cation disorder in transition-metal oxides. *Phys. Rev. Lett.* **119**, 176402 (2017).
19. Etcheri, V., Marom, R., Elazi, R., Salitra, G. & Aurbach, D. Challenges in the development of advanced Li-ion batteries: a review. *Energy Environ. Sci.* **4**, 3243–3262 (2011).
20. Wang, R. et al. A disordered rock-salt Li-excess cathode materials with high capacity and substantial oxygen redox activity: Li$_{1.25}$Nb$_{0.25}$Mn$_{0.5}$O$_2$. *Electrochem. Commun.* **60**, 70–73 (2015).
21. Yabuuchi, N. et al. Origin of stabilization and destabilization in solid-state redox reaction of oxide ions for lithium-ion batteries. *Nat. Commun.* **7**, 13814 (2016).
22. Lee, J. et al. A new class of high capacity cation-disordered oxides for rechargeable lithium batteries: Li–Ni–Ti–Mo oxides. *Energy Environ. Sci.* **8**, 3255–3265 (2015).
23. Manceau, A., Marcus, M. A. & Grangeon, S. Determination of Mn valence states in mixed-valent manganates by XANES spectroscopy. *Am. Mineral.* **97**, 816–827 (2012).
24. de Groot, F. M. F. et al. Oxygen 1*s* X-ray-absorption edges of transition-metal oxides. *Phys. Rev. B* **40**, 5715–5723 (1989).
25. Kurata, H., Lefèvre, E. & Colliex, C. Electron-energy-loss near-edge structures in the oxygen K-edge spectra of transition-metal oxides. *Phys. Rev. B* **47**, 13763–13768 (1993).
26. Luo, K. et al. Charge-compensation in 3*d*-transition-metal-oxide intercalation cathodes through the generation of localized electron holes on oxygen. *Nat. Chem.* **8**, 684–691 (2016).
27. Seo, D.-H. et al. The structural and chemical origin of the oxygen redox activity in layered and cation-disordered Li-excess cathode materials. *Nat. Chem.* **8**, 692–697 (2016).
28. Xie, Y., Saubanère, M. & Doublet, M.-L. Requirements for reversible extra-capacity in Li-rich layered oxides for Li-ion batteries. *Energy Environ. Sci.* **10**, 266–274 (2017).
29. Lee, J. et al. Mitigating oxygen loss to improve the cycling performance of high capacity cation-disordered cathode materials. *Nat. Commun.* **8**, 981 (2017).
30. Abdellahi, A., Urban, A., Dacek, S. & Ceder, G. Understanding the effect of cation disorder on the voltage profile of lithium transition-metal oxides. *Chem. Mater.* **28**, 5373–5383 (2016).
31. Cho, J., Kim, T.-J., Kim, Y. J. & Park, B. Complete blocking of Mn^{3+} ion dissolution from a LiMn$_2$O$_4$ spinel intercalation compound by Co$_3$O$_4$ coating. *Chem. Commun.* 1074–1075 (2001).
32. Xu, K. Electrolytes and interphases in Li-ion batteries and beyond. *Chem. Rev.* **114**, 11503–11618 (2014).
33. Wang, Y. et al. Design principles for solid-state lithium superionic conductors. *Nat. Mater.* **14**, 1026–1031 (2015).

METHODS

Synthesis. To synthesize $Li_2Mn_{2/3}Nb_{1/3}O_2F$, we used Li_2O (Sigma-Aldrich, 97%), MnO (Alfa Aesar, 99%), Nb_2O_5 (Alfa Aesar, 99.9%) and LiF (Alfa Aesar, 99.99%) as precursors. For $Li_2Mn_{1/2}Ti_{1/2}O_2F$, we used Li_2O (Sigma-Aldrich, 97%), MnO (Alfa Aesar, 99%), TiO_2 (Alfa Aesar, 99.9%) and LiF (Alfa Aesar, 99.99%) as precursors. Other than Li_2O, for which we used 10% excess (rather than stoichiometric amount) to compensate for possible loss of Li_2O during synthesis, stoichiometric amounts of precursors were dispersed into (Ar-filled) stainless steel jars and then planetary ball-milled (Retch PM 200) for 40 h at the rate of 450 r.p.m., during which $Li_2Mn_{2/3}Nb_{1/3}O_2F$ or $Li_2Mn_{1/2}Ti_{1/2}O_2F$ form mechanochemically. The total amount of precursors in each jar (50 ml) was approximately 1 g, and five 10-mm-diameter and ten 5-mm-diameter stainless balls were used as the grinding media.

Electrochemistry. To prepare a cathode film from $Li_2Mn_{2/3}Nb_{1/3}O_2F$ or $Li_2Mn_{1/2}Ti_{1/2}O_2F$, 480 mg of active compounds and 240 mg of carbon black (Timcal, SUPER C65) were first mixed for an hour in an Ar-filled 45-ml zirconia vial with 10 g of 5-mm-diameter yttria-stabilized zirconia balls (Inframat Advanced Materials) as grinding media, using a SPEX 8000M Mixer/Mill. Polytetrafluoroethylene (PTFE, DuPont, Teflon 8 A) was then added to the mixture as a binder, such that the cathode film consists of the active compounds, carbon black and PTFE in the weight ratio of 60:30:10. The weight ratio for cathode films with higher active-material loading was either 70:20:10 or 80:15:5. The components were then manually mixed using a mortar and pestle and rolled into a thin film inside an Ar-filled glove box. To assemble a cell for all cycling tests, 1 M of $LiPF_6$ in ethylene carbonate and dimethyl carbonate (EC/DMC) solution (1:1, BASF), glass microfibre filters (Whatman) and Li metal foil (FMC) were used as the electrolyte, the separator and the counter electrode, respectively. Coin cells (CR2032) were assembled in an Ar-filled glove box and tested on a Maccor 2200 or an Arbin battery cycler at room temperature in the galvanostatic mode otherwise specified. The loading density of the cathode film was about $6\,mg\,cm^{-2}$. The specific capacity was calculated on the amount of the active compounds in the cathode film.

Characterization. XRD patterns of the as-prepared compounds and electrodes were collected on a Rigaku MiniFlex diffractometer (Cu source) in the 2θ range of 5°–85°. Rietveld refinement was completed with PANalytical X'pert HighScore Plus software. Elemental analysis on the compounds by Luvak Inc. was performed with direct current plasma emission spectroscopy (ASTM E 1097-12) for Li, Mn, Nb and Ti, and with an ion-selective electrode (ASTM D1179-10) for F. SEM images were collected on a Zeiss Gemini Ultra-55 Analytical Field Emission SEM in the Molecular Foundry at Lawrence Berkeley National Laboratory (LBNL). For TEM sampling, particles are sonicated with ethanol and drop-cast on an ultrathin carbon grid. Scanning TEM/EDS spectra were acquired from a few of the particles on a JEM-2010F microscope equipped with an X-max EDS detector in the Molecular Foundry at LBNL.

Hard X-ray absorption spectroscopy. We performed Mn, Nb and Ti K-edge XANES measurements in transmission mode using beamline 20BM at the Advanced Photon Source. The incident energy was selected using a Si(111) monochromator. We performed the energy calibration by simultaneously measuring the spectra of the appropriate metal foil. Harmonic rejection was accomplished using a Rh-coated mirror. The samples for the measurements were prepared with the $Li_2Mn_{2/3}Nb_{1/3}O_2F$ and $Li_2Mn_{1/2}Ti_{1/2}O_2F$ electrode films before and after first charging and discharging to designated capacities. The loading density of the films was approximately $10\,mg\,cm^{-2}$. Additionally, we measured the spectra of some reference standards in transmission mode, to aid interpretation of the XANES data. Data reduction was carried out using the Athena software[34].

Soft X-ray absorption spectroscopy. Soft XAS measurements on the O K-edge were performed on Beamline 8.0.1.1 (iRIXS endstation) at the Advanced Light Source, LBNL[35]. All the O K-edge XAS spectra were normalized by incident beam flux monitored by a gold mesh, which was located in front of the ultra-high-vacuum experimental chamber. The energy resolution of the O K-edge XAS spectra was set to 0.2 eV and a reference (anatase) TiO_2 O K-edge XAS spectrum was also recorded for careful energy calibration during the XAS experiments. XAS spectra taken in total fluorescence yield mode were chosen and presented as Fig. 3c in this paper to represent the bulk-like information (typically a few hundred nanometres below the sample surface) from these cathode materials. In addition, sample preparation and handling for X-ray spectroscopy were done in an air-free environment to avoid surface contamination and oxidation.

Differential electrochemical mass spectrometer measurement. A DEMS measurement was used to detect and quantify O_2 and CO_2 gas evolved during charging and discharging (Extended Data Fig. 5). The custom-built DEMS and the cell geometry used are described in previous publications[36–38]. The electrochemical cells used with the DEMS device were prepared in a dry Ar glove box (<1 ppm O_2 and H_2O, MBraun USA, Inc.) using the modified Swagelok design and the same materials as discussed previously. The assembled cells were charged under a static head of positive Ar pressure (approximately 1.2 bar) after being appropriately attached to the DEMS. Throughout the charge, Ar gas pulses periodically swept accumulated gases to a mass spectrometer chamber. The mass spectrometer absolute sensitivity has been calibrated for CO_2 and O_2, and therefore the partial pressures of these gases can be determined. The amount of CO_2 and O_2 evolved is then quantified based on the volume of gas swept to the mass spectrometer per pulse.

Solid-state NMR spectroscopy. We acquired all ^7Li and ^{19}F NMR data at room temperature on a Bruker Avance500 WB spectrometer (11.7 T), at Larmor frequencies of −194.4 and −70.7 MHz, respectively. The data were obtained under 50-kHz magic-angle spinning (MAS), using a 1.3-mm double-resonance probe. The chemical shifts of ^7Li and ^{19}F were referenced against lithium fluoride powder (LiF, $\delta_{iso}(^7Li) = -1$ ppm and $\delta_{iso}(^{19}F) = -204$ ppm). ^7Li spin echo spectra were acquired on as-synthesized $Li_2Mn_{2/3}Nb_{1/3}O_2F$ and $Li_2Mn_{1/2}Ti_{1/2}O_2F$ using a 90° radio-frequency (RF) excitation pulse of 0.9 μs and a 180° RF pulse of 1.8 μs at 110 W. A recycle delay of 0.03 s was found to be sufficiently long to ensure complete relaxation of all Li signals between the excitation pulses. Lineshape analysis was carried out using the SOLA lineshape simulation package within the Bruker TOPSPIN software. Because the resonant frequency range of the ^{19}F nuclei in the as-synthesized $Li_2Mn_{2/3}Nb_{1/3}O_2F$ and $Li_2Mn_{1/2}Ti_{1/2}O_2F$ samples is larger than the excitation bandwidth of the RF pulse used in the NMR experiment, nine spin echo spectra were collected on each sample, with the irradiation frequency varied in steps equal to the excitation bandwidth of the RF pulse (330 ppm or 155 kHz). The individual sub-spectra were processed using zero-order phase correction so that the on-resonance signal was in the absorption mode. The nine sub-spectra were then added to give an overall sum spectrum with no further phase correction required. We note that this methodology, termed 'spin echo mapping'[39], 'frequency stepping'[40,41] or 'VOCS' (variable offset cumulative spectrum)[42], is required to provide a large excitation bandwidth and uniformly excite the broad F signals. Individual ^{19}F spin echo spectra were collected using a 90° RF excitation pulse of 1.6 μs and a 180° RF pulse of 3.2 μs at 76.3 W (or 156 kHz), with a recycle delay of 0.05 s. For comparison, a spin echo spectrum was collected on LiF using similar RF pulses but a longer recycle delay of 14 s. A ^{19}F spin echo spectrum, acquired under the same conditions as the $Li_2Mn_{2/3}Nb_{1/3}O_2F$ and $Li_2Mn_{1/2}Ti_{1/2}O_2F$ spin echo spectra but on an empty rotor, revealed no significant background signal coming from the NMR probe itself.

Density functional theory calculations. Density functional theory analysis of the redox mechanism was performed with the Vienna Ab-Initio Simulation Package (VASP)[43] using the projector augmented-wave method. First, structural models of the $Li_2Mn_{2/3}Nb_{1/3}O_2F$ disordered rocksalt were obtained using a cluster-expansion-based Monte Carlo simulation, chosen to find low-energy disordered structures with representative short-range order, while suppressing phase separation. The cluster-expansion Hamiltonian used for the Monte Carlo simulations consists of a decomposition of the internal energy of a particular atomic configuration on a rocksalt lattice into contributions from two-, three-, and four-body terms up to maximum interaction distance of 7.0 Å, 4.1 Å and 4.1 Å respectively, relative to an ideal rocksalt lattice with a primitive lattice constant of 3.0 Å, on top of an electrostatic model based on the formal charges of all species[44]. To obtain the interaction terms, we first calculated 450 representative configurations of Li^+, Mn^{2+}, Nb^{5+}, O^{2-} and F^- on a rocksalt lattice within the Perdew–Burke–Ernzerhof exchange-correlation functional[45], supplemented with the rotationally invariant Hubbard U correction[46] to the transition metal d states to correct self-interaction error ($U_{Mn} = 3.9\,eV$, $U_{Nb} = 1.5\,eV$ based on previously reported fits to oxide formation enthalpies[47]). These calculations were performed with a reciprocal-space discretization of $25\,Å^{-1}$, 520 eV plane-wave cut-off, and a 10^{-5} eV and $0.02\,eV\,Å^{-1}$ convergence on total energy and interatomic forces respectively. The strength of each cluster interaction, as well as the dielectric constant, was then fitted using a L_1-regularized least-squares regression, optimized by cross-validation, which resulted in an out-of-sample error of 9 meV per atom.

The redox mechanism of $Li_2Mn_{2/3}Nb_{1/3}O_2F$ was calculated on 12 structural models of 36 atoms each, obtained from the Monte Carlo simulations described above. Oxidation calculations were done using the hybrid Heyd–Scuseria–Ernzerhof functional[48], using a 650-eV plane-wave cut-off, $10\,Å^{-1}$ reciprocal-space discretization, and a 10^{-5} eV and $0.02\,eV\,Å^{-1}$ convergence on total energy and interatomic forces respectively. The fraction of exact exchange was set to 0.30 on the basis of a calibration to the Kohn–Sham gaps of α-Mn_3O_4, γ-MnOOH and β-MnO_2 calculated within the G_0W_0 approximation, following previously reported methodology for reproducing the redox competition between transition metals and oxygen[49]. To investigate the order in which various redox couples are activated in the material, suppressing major structural rearrangements, we trace the oxidation state of each species (obtained from the magnetic moment of each atom) as electrons are removed from the material and charge compensated by a uniform background charge[50], allowing the local atomic arrangements to relax at each step but keeping the lattice fixed. As the order of oxidation reactions is determined by the character of the valence-band edge at various states of charge, such electron titration provides an efficient way to look at the electronic contribution to the redox mechanism.

Supplementary Note 1. The absence of peaks other than those corresponding to the disordered-rocksalt phases in the XRD data collected on as-synthesized $Li_2Mn_{2/3}Nb_{1/3}O_2F$ and $Li_2Mn_{1/2}Ti_{1/2}O_2F$ suggests that the samples are fairly phase-pure without large amounts of crystalline impurities such as LiF, Li_2O, or Li_2CO_3. Nevertheless, because small amounts of impurity phases or amorphous phases can be invisible to XRD, we investigated further using ^{7}Li and ^{19}F NMR spectroscopy.

^{7}Li spin echo NMR spectra, obtained on as-synthesized $Li_2Mn_{2/3}Nb_{1/3}O_2F$ and $Li_2Mn_{1/2}Ti_{1/2}O_2F$ samples, are shown in Extended Data Fig. 1a, b. The data have been fitted using a minimum of three Li sites: Li1, Li2 and Li3. The fits suggest about 78%–79% ($\pm$2%) of Li in paramagnetic environments (Li1 and Li2 signals), and about 21%–22% ($\pm$2%) Li in diamagnetic environments (Li3 signal). The broad Li1 and Li2 resonances are ascribed to several paramagnetic Li environments close to open-shell Mn and with very similar shifts, resulting in overlapping signals. Paramagnetic interactions between unpaired Mn d electrons and the Li nuclei lead to a broadening of the individual Li signals with shifts centred around 64.9 ppm (Li1) and −27.4 ppm (Li2) for $Li_2Mn_{1/2}Ti_{1/2}O_2F$, and around 57.7 ppm (Li1) and −25.5 ppm (Li2) for $Li_2Mn_{2/3}Nb_{1/3}O_2F$. The sharper Li3 resonance, with a shift close to 0 ppm (−0.1 ppm for $Li_2Mn_{1/2}Ti_{1/2}O_2F$ and −0.5 ppm for $Li_2Mn_{2/3}Nb_{1/3}O_2F$), is ascribed to diamagnetic Li sites in the samples. Because Li^+, Nb^{5+} and Ti^{4+} do not have unpaired electrons, Li nuclei in diamagnetic Li/Ti- and Li/Nb-rich domains in $Li_2Mn_{1/2}Ti_{1/2}O_2F$ and $Li_2Mn_{2/3}Nb_{1/3}O_2F$ have a shift around 0 ppm that cannot be distinguished from that of potential Li_2O, LiF and Li_2CO_3 impurities, resonating at 2.8, −1 and 0 ppm, respectively[51]. All of these Li environments may contribute to the Li3 signal, and individual contributions cannot be quantified. In fact, local segregation of cations that would lead to Li/Ti- or Li/Nb-rich domains in our compounds has been observed in several examples—for example, $LiMnO_3$-like domains in Li- and Mn-rich layered Ni–Mn–Co materials[10], or Li_3NbO_4-like local domains in disordered Li–V–Nb–O materials[52]. A previous ^{7}Li NMR study on paramagnetic Li transition metal phosphates ($LiMPO_4$) cathodes has found that paramagnetic shift contributions from distant M beyond the second metal coordination shell around the central Li can be non-zero[53]. This observation suggests that, in $Li_2Mn_{1/2}Ti_{1/2}O_2F$ and $Li_2Mn_{2/3}Nb_{1/3}O_2F$, Mn is likely to be more than 7 Å away from the Li for there to be no paramagnetic shift contribution and an overall Li shift close to 0 ppm.

[19]F spin echo sum spectra, collected on as-synthesized $Li_2Mn_{2/3}Nb_{1/3}O_2F$ and $Li_2Mn_{1/2}Ti_{1/2}O_2F$, are compared to the spin echo spectrum collected on crystalline LiF powder and presented in the Extended Data Fig. 1c. Further details on how the sum spectra were obtained can be found in the Methods section for solid state NMR spectroscopy where we describe the method of 'spin echo mapping'. The ^{19}F NMR data clearly indicate that most of the F is found in paramagnetic environments (that is, with Mn in the first, second and/or third metal coordination shell around the F nucleus), giving rise to very broad overlapping NMR signals shifted away from the LiF resonant frequency. Nevertheless, LiF-like F environments are also observed as a sharp signal with a resonant frequency equal to that of pure LiF (−204 ppm). Some of our current work on similar paramagnetic cation-disordered oxyfluorides suggests that F nuclei directly bonded to the paramagnetic centre (here Mn) are essentially invisible in the NMR spectrum, because the very strong interaction with the unpaired electrons leads to extremely broad resonances with a very large shift that are lost in the background. Hence, we suspect our ^{19}F NMR data not to be quantitative and the proportion of F in paramagnetic environments to be even larger than that determined from experimental observations. With this in mind, the ^{19}F NMR data confirm that most of the F has integrated into the bulk cation-disordered oxide lattice. Although the −204 ppm ^{19}F signal can indicate LiF impurity in our samples, it can also indicate the presence of a small proportion of LiF-like domains in the disordered oxyfluoride structure, which would be consistent with recent theory work[15] showing that the much higher energetic cost of creating M–F bonds, as compared with Li–F bonds, results in the incorporation of F in Li-rich (that is, LiF-like) local environments in cation-disordered oxyfluoride materials.

In short, diamagnetic Li sites and LiF-like F environments observed with NMR cannot be uniquely attributed to either local domains in the rocksalt structure or to amorphous impurity phases, such as LiF, Li_2O or Li_2CO_3, in our samples. Hence, NMR can give us an upper bound to the amount of impurity present in the samples but does not enable us to obtain the exact amount of potential impurity phases. In the extreme case in which all of the diamagnetic Li and LiF-like F signals come from Li_2O and LiF, the total weight fraction of impurity phases is estimated to be no more than 6–7 wt%; it is likely to be less, as no crystalline impurities were observed with XRD and no amorphous domains were observed in TEM (Extended Data Figs. 2, 9). As a result, we are confident stating that the performance of $Li_2Mn_{2/3}Nb_{1/3}O_2F$ and $Li_2Mn_{1/2}Ti_{1/2}O_2F$ is predominantly determined by the transition metal oxyfluoride rocksalt phase.

Supplementary Note 2. Extended Data Fig. 5a, b shows the O_2 (g) and CO_2 (g) evolution data from $Li_2Mn_{2/3}Nb_{1/3}O_2F$ and $Li_2Mn_{1/2}Ti_{1/2}O_2F$ during initial charge (1.5–5.0 V, 20 mA g^{-1}), collected by DEMS measurements. The capacity observed

during this DEMS test is slightly smaller than that in a coin cell test, because the electrode films were made thicker (about 13 mg cm^{-2} versus about 6 mg cm^{-2} in coin cells) for this measurement to enhance gas evolution signals. We detect negligible O_2 (g) evolution from both compounds upon first charging to 5 V. The total amount of O_2 (g) evolved during the first charge is smaller than 0.01 μmol mg^{-1} (of active material) for both $Li_2Mn_{2/3}Nb_{1/3}O_2F$ and $Li_2Mn_{1/2}Ti_{1/2}O_2F$, which corresponds to less than 0.2% of total oxygen content in the two materials. For conventional layered Li- and Mn-rich cathodes, such as $Li_{1.2}Ni_{0.13}Co_{0.13}Mn_{0.54}O_2$, oxygen loss occurs dominantly in the form of O_2 (g) evolution which starts from above 4.5 V in the first charge, and results in a loss of about 4%–5% of the total oxygen content of the cathode materials[10,26]. Therefore, the remarkably small amount of O_2 (g) evolved even until 5 V demonstrates negligible oxygen loss from both $Li_2Mn_{2/3}Nb_{1/3}O_2F$ and $Li_2Mn_{1/2}Ti_{1/2}O_2F$ compounds.

Interestingly, we detect a noticeable amount of CO_2 (g) evolved from the two materials (0.30 μmol mg^{-1} and 0.24 μmol mg^{-1} for $Li_2Mn_{2/3}Nb_{1/3}O_2F$ and $Li_2Mn_{1/2}Ti_{1/2}O_2F$, respectively), with much of the evolved CO_2 coming at lower voltages than the threshold voltage (about 4.5 V) for decomposition of 1 M $LiPF_6$ in EC/DMC electrolyte[32]. On the basis of an acid titration test using 1 M H_2SO_4[54,55], we find that most of this CO_2 (g) is likely to come from electrochemical decomposition of surface carbonates (for example solid lithium carbonate) that probably form during the shaker-milling process between the active compounds and carbon black. For instance, Extended Data Fig. 5c shows the cumulative CO_2 evolution during acid titration on shaker-milled $Li_2Mn_{1/2}Ti_{1/2}O_2F$ and carbon black mixture. CO_2 (g) evolves from the mixture immediately after adding 1 M H_2SO_4, with a total CO_2 amount of about 0.17 μmol per mg of $Li_2Mn_{1/2}Ti_{1/2}O_2F$. This direct CO_2 evolution indicates a chemical decomposition of an equimolar amount of carbonate species by the H_2SO_4 addition (about 0.7 wt% of the powder mixture, assuming Li_2CO_3 as the carbonate species), which can also decompose electrochemically. Since 5 V is a high enough voltage to electrochemically decompose carbonates[32,55], we expect that a similar amount of CO_2 (g) to that in the acid titration would evolve from the surface carbonates during charging of the $Li_2Mn_{1/2}Ti_{1/2}O_2F$ electrode, which would imply that about 71% (about 0.17 μmol mg^{-1} out of 0.24 μmol mg^{-1}) of the CO_2 evolved during the first charge originates from carbonate decomposition.

It is worth noting that some sub-surface Li_2CO_3 may not be detected using our acid titration method, although this carbonate may still oxidize to CO_2 during the first charge cycle such that carbonate oxidation accounts for nearly all CO_2 evolution observed in Extended Data Fig. 5a, b. From the many transition metal oxides studied using our gas evolution methods (for example, Ni-rich and Li/Mn-rich Ni–Mn–Co oxides)[55], residual Li_2CO_3, and not electrolyte degradation (below 4.8 V), has accounted for all CO_2 evolution during the first charge cycle, and it is likely that a similar phenomenon is observed for these materials. Nevertheless, it is possible, although less likely, that the additional CO_2 evolved beyond that expected from the titrated Li_2CO_3 quantity may come from direct electrolyte decomposition, particularly at high voltages (>4.8 V), or from some oxygen species evolved from the materials reacting with the electrolyte[26,32,55,56].

Supplementary Note 3. Most of the Li-excess Mn-rich cathodes using high levels of oxygen redox experience voltage fading, a continuous reduction of both charge and discharge voltages upon extended cycling[10,57]. From the evolution of average voltages upon cycling (Extended Data Fig. 6), we find that voltage fading for $Li_2Mn_{2/3}Nb_{1/3}O_2F$ is less pronounced than for other Mn-rich cathodes. Comparing the 2nd and 20th cycles between 1.5 and 4.6 V, 1.5 and 4.8 V, and 1.5 and 5.0 V at 20 mA g^{-1}, we observe a decrease of the average discharge voltage by approximately 1.3%, 2.2% and 4.0%, respectively. Apparently, a higher charge cut-off voltage results in more reduction of discharge voltage upon cycling. On the contrary, the average charge voltage increases by about 1.8%, 1.3%, and 1.9%, when comparing the 2nd and 20th cycles between 1.5 and 4.6 V, 1.5 and 4.8 V, and 1.5 and 5.0 V, respectively. In fact, half of the average charge–discharge voltages ((charge voltage + discharge voltage)/2) changes only about 0.3%, 0.27% and 0.7%, when comparing the 2nd and 20th cycles between 1.5 and 4.6 V, 1.5 and 4.8 V, and 1.5 and 5.0 V, respectively. For the Mn-rich Li-excess materials that experience voltage fading, both the discharge and charge voltages decrease upon cycling[10,57]. Our result, on the other hand, shows slight decrease of discharge voltage but increase of charge voltage, and the average of the two barely changes. This indicates that the voltage change for $Li_2Mn_{2/3}Nb_{1/3}O_2F$ is unlikely to be the result of irreversible voltage fading but is the result of impedance growth such as from electrolyte decomposition at high voltages above 4.5 V[32].

Supplementary Note 4. We performed hard XAS on the $Li_2Mn_{2/3}Nb_{1/3}O_2F$ material. Along with rising edges (Extended Data Fig. 7a), pre-edge features of XANES spectra (Extended Data Fig. 7b) can give information about oxidation states. The pre-edge feature (about 6,539 eV) in the Mn K-edge XANES spectra originates from electron excitation from the Mn $1s$ state to mixed Mn $3d$–$4p$ states, allowed in a non-centrosymmetric environment[58]. Direct comparison of the Mn K-edge pre-edge features of $Li_2Mn_{2/3}Nb_{1/3}O_2F$ upon cycling is shown in Extended Data Fig. 7b. To analyse their shape more clearly, first derivatives of their pre-edges are

shown in Extended Data Fig. 7c–e. The first derivatives of the spectra from 'before cycle' and 'after first charging to 375 mAh g^{-1} then discharging to 320 mAh g^{-1}' resemble that of MnO (Extended Data Fig. 7c), suggesting that most Mn ions in the two samples are in the Mn^{2+} state. After first charging $Li_2Mn_{2/3}Nb_{1/3}O_2F$ to 135 mAh g^{-1}, the derivative shape looks similar to that of Mn_2O_3, indicating the presence of Mn^{3+} in the sample (Extended Data Fig. 7d). After charging to 270 and 360 mAh g^{-1}, the derivative shape changes towards that of MnO_2, indicating mostly Mn^{4+} ions although Mn^{3+} and Mn^{2+} might also be present (Extended Data Fig. 7e).

Supplementary Note 5. $Li_2Mn_{1/2}Ti_{1/2}O_2F$ exhibits promising cycling behaviour, as does $Li_2Mn_{2/3}Nb_{1/3}O_2F$. When cycled between 1.6 V and 5.0 V (Extended Data Fig. 10a), 2.0 V and 4.8 V (Extended Data Fig. 10b), and 2.3 V and 4.6 V (Extended Data Fig. 10c) at 20 mA g^{-1}, the 60 wt%:30 wt%:10 wt% = $Li_2Mn_{1/2}Ti_{1/2}O_2F$: carbon black:PTFE electrode delivers discharge capacities up to 306 mAh g^{-1} (920 Wh kg^{-1}), 227 mAh g^{-1} (739 Wh kg^{-1}), and 160 mAh g^{-1} (534 Wh kg^{-1}), respectively. Rate capability of $Li_2Mn_{1/2}Ti_{1/2}O_2F$ is acceptable. When cycled at high rates of 200 and 400 mA g^{-1} between 1.6 V and 5.0 V, the material still delivers discharge capacities up to 210 mAh g^{-1} (629 Wh kg^{-1}) and 158 mAh g^{-1} (461 Wh kg^{-1}) (Extended Data Fig. 10d). Capacity retention of $Li_2Mn_{1/2}Ti_{1/2}O_2F$ (Extended Data Fig. 7e) is good and is slightly better than that of $Li_2Mn_{2/3}Nb_{1/3}O_2F$ (Extended Data Fig. 4). When cycled at 100 mA g^{-1} and above, the capacity loss during initial 25 cycles is less than 0.4% per cycle. The 80 wt%:15 wt%:5 wt% = $Li_2Mn_{1/2}Ti_{1/2}O_2F$:carbon black:PTFE electrode exhibits similar performance to the 60 wt%:30 wt%:10 wt% = $Li_2Mn_{1/2}Ti_{1/2}O_2F$:carbon black:PTFE electrode (Extended Data Fig. 10b, f).

Supplementary Note 6. Extended Data Fig. 11a, b shows the Mn K-edge XANES spectra of $Li_2Mn_{1/2}Ti_{1/2}O_2F$ before cycle, after charging to 120 mAh g^{-1}, 240 mAh g^{-1} and 400 mAh g^{-1}, and after charging to 400 mAh g^{-1} then discharging to 330 mAh g^{-1}. Upon first charging from 0 to 120 mAh g^{-1} and 240 mAh g^{-1}, the Mn rising-edge shifts, from an energy in between those in MnO and Mn_2O_3, to an energy in Mn_2O_3 and then partway up to an energy in MnO_2. Further change is small upon charging to 400 mAh g^{-1}. The edge returns to the original position after discharging to 330 mAh g^{-1}. This result suggests that Mn ions in the as-prepared $Li_2Mn_{1/2}Ti_{1/2}O_2F$ compounds are mostly Mn^{2+} (possibly with some Mn^{3+}), which are oxidized in charge towards Mn^{4+} with some Mn ions not fully oxidized. Upon discharge, Mn ions return to Mn^{2+}. Note that because the shape of Mn K-edge spectra for a given oxidation state can vary a lot depending on bonding environment[58], and there are no reported references for Mn-based disordered-oxyfluoride compounds, quantitative analysis of our results is difficult.

Derivative analysis on the Mn pre-edge feature at about 6,539 eV (Extended Data Fig. 11c–e) suggests the same Mn-redox mechanism. The first derivatives of the spectra from 'before cycle' and 'after first charging to 400 mAh g^{-1} then discharging to 330 mAh g^{-1}' exhibit a mixed shape of the first-derivative spectra of MnO and Mn_2O_3 (Extended Data Fig. 11c). This suggests an existence of Mn^{2+} ions with some partly oxidized Mn ions such as Mn^{3+}. After first charging to 120 mAh g^{-1}, the derivative shape looks similar to that of Mn_2O_3, indicating Mn^{3+} in the sample (Extended Data Fig. 11d). After charging to 240 and 400 mAh g^{-1}, the derivative shape changes towards that of MnO_2, suggesting a large amount of Mn^{4+} ions, but Mn^{3+} and Mn^{2+} might also be present (Extended Data Fig. 11e).

The Ti K-edge spectra of the $Li_2Mn_{1/2}Ti_{1/2}O_2F$ samples (Extended Data Fig. 11f) resemble that of TiO_2 (Ti^{4+}) and their rising-edge position barely changes during cycling, although there are minor changes in shape, which indicates local Ti-site distortion[59]. This suggests that Ti exists as Ti^{4+} and is redox-silent. Because Ti^{4+} is redox inactive, we expect that reversible capacities of $Li_2Mn_{1/2}Ti_{1/2}O_2F$ beyond Mn capacities come from O redox, as in the case of $Li_2Mn_{2/3}Nb_{1/3}O_2F$.

Data availability. The datasets generated and analysed during this study are available from the corresponding authors on reasonable request.

34. Ravel, B. & Newville, M. ATHENA, ARTEMIS, HEPHAESTUS: data analysis for X-ray absorption spectroscopy using IFEFFIT. *J. Synchrotron Radiat.* **12**, 537–541 (2005).

35. Yang, W. et al. Key electronic states in lithium battery materials probed by soft X-ray spectroscopy. *J. Electron Spectrosc. Relat. Phenom.* **190**, 64–74 (2013).

36. McCloskey, B. D., Bethune, D. S., Shelby, R. M., Girishkumar, G. & Luntz, A. C. Solvents' critical role in nonaqueous lithium–oxygen battery electrochemistry. *J. Phys. Chem. Lett.* **2**, 1161–1166 (2011).

37. McCloskey, B. D. et al. On the efficacy of electrocatalysis in nonaqueous Li-O$_2$ batteries. *J. Am. Chem. Soc.* **133**, 18038–18041 (2011).

38. McCloskey, B. D. et al. Twin problems of interfacial carbonate formation in nonaqueous Li-O$_2$ batteries. *J. Phys. Chem. Lett.* **3**, 997–1001 (2012).

39. Sananes, M. T., Tuel, A., Hutchings, G. J. & Volta, J. C. Characterization of different precursors and activated vanadium phosphate catalysis by ^{31}P NMR spin echo mapping. *J. Catal.* **148**, 395–398 (1994).

40. O'Dell, L. A. & Schurko, R. W. QCPMG using adiabatic pulses for faster acquisition of ultra-wideline NMR spectra. *Chem. Phys. Lett* **464**, 97–102 (2008).

41. Pell, A. J., Clément, R. J., Grey, C. P., Emsley, L. & Pintacuda, G. Frequency-stepped acquisition in nuclear magnetic resonance spectroscopy under magic angle spinning. *J. Chem. Phys.* **138**, 114201 (2013).

42. Massiot, D. et al. ^{71}Ga and ^{69}Ga nuclear magnetic resonance study of β-Ga$_2$O$_3$: resolution of four- and six-fold coordinated Ga sites in static conditions. *Solid State Nucl. Magn. Reson.* **4**, 241–248 (1995).

43. Kresse, G. & Furthmüller, J. Efficient iterative schemes for ab initio total-energy calculations using a plane-wave basis set. *Phys. Rev. B* **54**, 11169–11186 (1996).

44. Richards, W. D., Wang, Y., Miara, L., Kim, J. C. & Ceder, G. Design of Li$_{1+2x}$Zn$_{1-x}$PS$_4$, a new lithium ion conductor. *Energy Environ. Sci.* **9**, 3272–3278 (2016).

45. Perdew, J. P., Burke, K. & Ernzerhof, M. Generalized gradient approximation made simple. *Phys. Rev. Lett.* **77**, 3865–3868 (1996).

46. Dudarev, S., Botton, G. A., Savrasov, S. Y. & Sutton, A. P. Electron-energy-loss spectra and the structural stability of nickel oxide: an LSDA+U study. *Phys. Rev. B* **57**, 1505–1509 (1998).

47. Wang, L., Maxisch, T. & Ceder, G. Oxidation energies of transition metal oxides within the GGA+U framework. *Phys. Rev. B* **73**, 8627 (1994).

48. Heyd, J., Scuseria, G. E. & Ernzerhof, M. Hybrid functionals based on a screened coulomb potential. *J. Chem. Phys.* **118**, 8207 (2003).

49. Seo, D.-H., Urban, A. & Ceder, G. Calibrating transition-metal energy levels and oxygen bands in first-principles calculations: accurate prediction of redox potentials and charge transfer in lithium transition-metal oxides. *Phys. Rev. B* **92**, 115118 (2015).

50. Raebiger, H., Lany, S. & Zunger, A. Charge self-regulation upon changing the oxidation state of transition metals in insulators. *Nature* **453**, 763–766 (2008).

51. Dupré, N., Cuisinier, M. & Guyomard, D. Electrode/electrolyte interface studies in lithium batteries using NMR. *Electrochem. Soc. Interface* **20**, 61–67 (2011).

52. Nakajima, M. & Yabuuchi, N. Lithium-excess cation-disordered rocksalt-type oxide with nanoscale phase segregation: Li$_{1.25}$Nb$_{0.25}$V$_{0.5}$O$_2$. *Chem. Mater.* **29**, 6927–6935 (2017).

53. Middlemiss, D. S., Iliott, A. J., Clément, R. J., Strobridge, F. C. & Grey, C. P. Density functional theory-based bond pathway decompositions of hyperfine shifts: equipping solid-state NMR to characterize atomic environments in paramagnetic materials. *Chem. Mater.* **25**, 1723–1734 (2013).

54. McCloskey, B. D. et al. Combining accurate O$_2$ and Li$_2$O$_2$ assays to separate discharge and charge stability limitations in nonaqueous Li–O$_2$ batteries. *J. Phys. Chem. Lett.* **4**, 2989–2993 (2013).

55. Renfrew, S. & McCloskey, B. D. Residual lithium carbonate predominantly accounts for first cycle CO$_2$ and CO outgassing of Li-stoichiometric and Li-rich layered transition-metal oxides. *J. Am. Chem. Soc.* **139**, 17853–17860 (2017).

56. Yabuuchi, N., Yoshii, J., Myung, S.-T., Nakai, I. & Komaba, S. Detailed studies of a high-capacity electrode material for rechargeable batteries, Li$_2$MnO$_3$–LiCo$_{1/3}$Ni$_{1/3}$Mn$_{1/3}$O$_2$. *J. Am. Chem. Soc.* **133**, 4404–4419 (2011).

57. Bettge, M. et al. Voltage fade of layered oxides: its measurement and impact on energy density. *J. Electrochem. Soc.* **160**, A2046–A2055 (2013).

58. Chalmin, E., Farges, F. & Brown, G. E. Jr. A pre-edge analysis of Mn K-edge XANES spectra to help determine the speciation of manganese in minerals and glasses. *Contrib. Mineral. Petrol.* **157**, 111–126 (2009).

59. Farges, F., Brown, G. E. Jr & Rehr, J. J. Coordination chemistry of Ti(IV) silicate glasses and melts: XAFS study of titanium coordination in oxide model compounds. *Geochim. Cosmochim. Acta* **60**, 3023–3038 (1996).

60. Piilonen, P. C. et al. Structural environment of Nb^{5+} in dry and fluid-rich (H$_2$O, F) silicate glasses: a combined XANES and EXAFS study. *Can. Mineral.* **44**, 775–794 (2006).
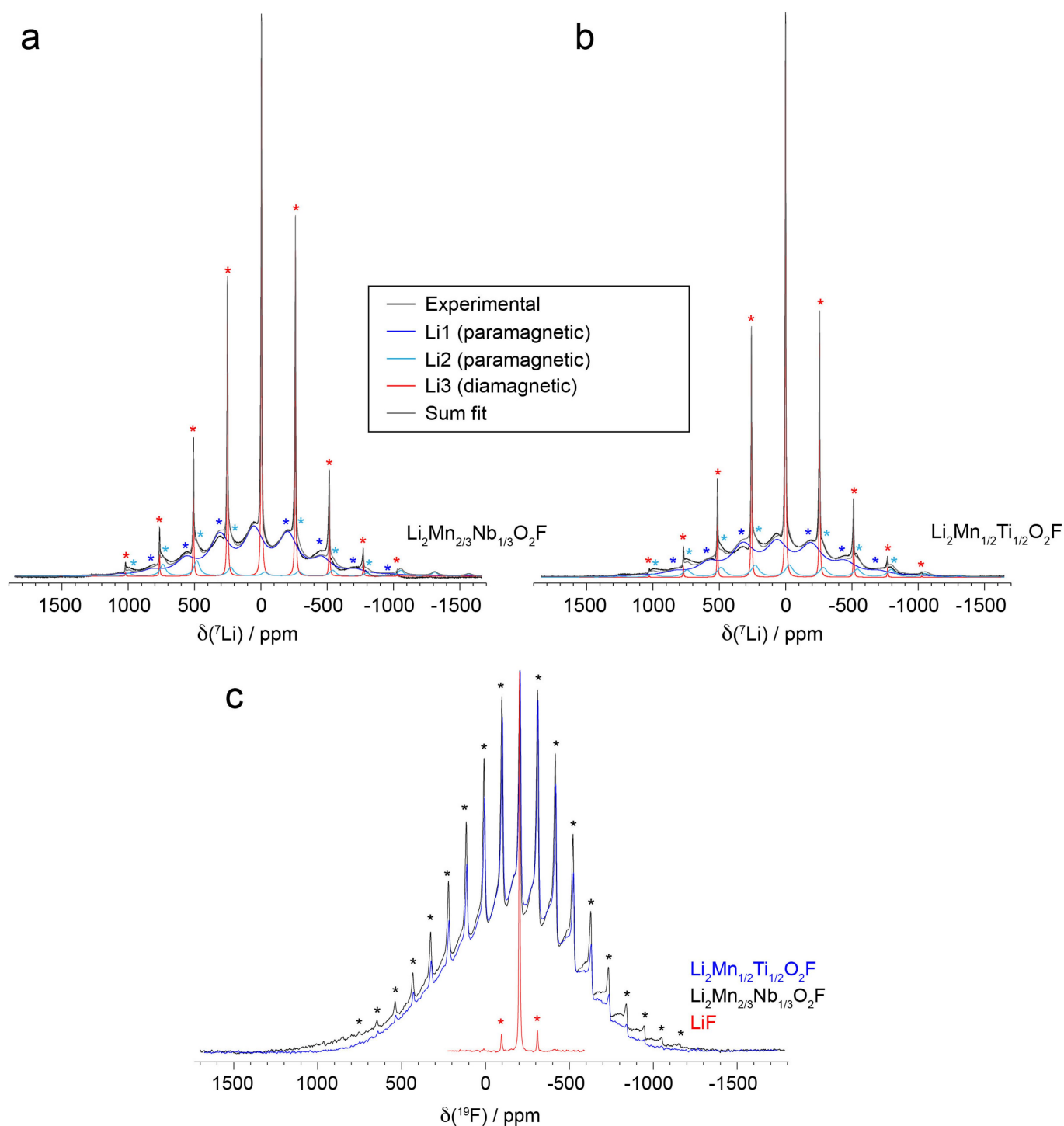
**Extended Data Fig. 1 | Solid-state NMR spectroscopy results. a, b,** ^{7}Li spin echo NMR spectra acquired on as-synthesized $Li_2Mn_{2/3}Nb_{1/3}O_2F$ (**a**) and $Li_2Mn_{1/2}Ti_{1/2}O_2F$ (**b**) powders at 50 kHz MAS at a field $B_0 = 11.7$ T. The data have been fitted with a minimal number of Li sites: Li1, Li2 and Li3. Spinning sidebands of the three Li signals are indicated with asterisks. **c,** ^{19}F spin echo sum spectra acquired on as-synthesized $Li_2Mn_{2/3}Nb_{1/3}O_2F$ and $Li_2Mn_{1/2}Ti_{1/2}O_2F$ powders at 50 kHz MAS at a field $B_0 = 11.7$ T. The spectra are compared to the spin echo spectrum collected on LiF under similar conditions. Spinning sidebands of the sharp LiF-like signals are indicated with asterisks. Detailed explanations of the results are given in Methods section 'Supplementary Note 1'.
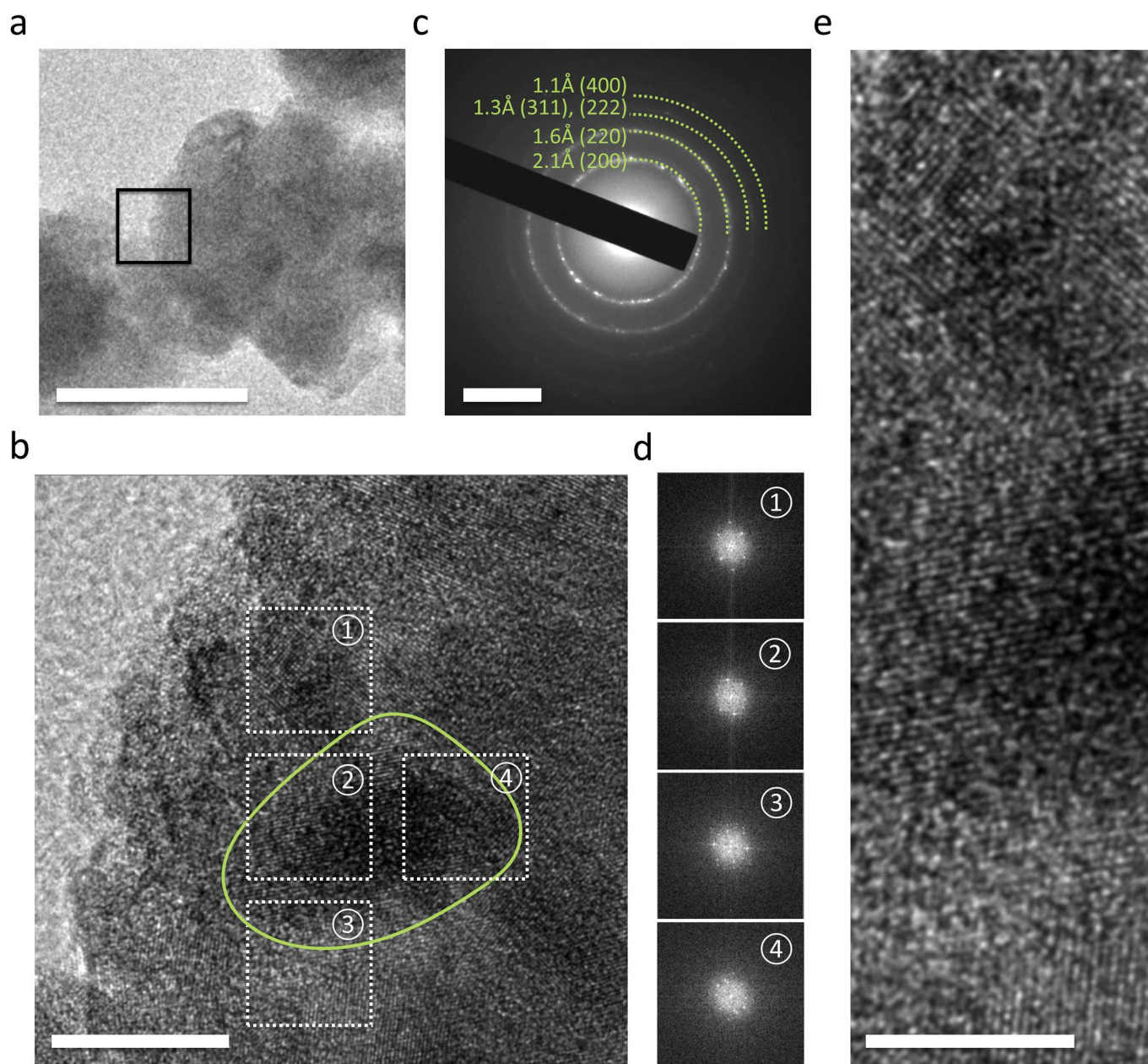
Extended Data Fig. 2 | Structural characterization of Li$_2$Mn$_{2/3}$Nb$_{1/3}$O$_2$F.
a, TEM image of as-synthesized Li$_2$Mn$_{2/3}$Nb$_{1/3}$O$_2$F particles. Scale bar, 50 nm. **b**, A high-magnification TEM image of the area enclosed in a square in **a**. Scale bar, 10 nm. The yellow circle indicates the boundary of one of the many grains in the polycrystalline Li$_2$Mn$_{2/3}$Nb$_{1/3}$O$_2$F particle. **c**, An electron diffraction pattern of the Li$_2$Mn$_{2/3}$Nb$_{1/3}$O$_2$F particle.

Scale bar, 5 nm^{-1}. **d**, Fast Fourier-transformed (FFT) images of the dotted squared areas in **b**. **e**, The high magnification image across the squared areas 1, 2 and 3 in **b**. Scale bar, 5 nm. We can clearly observe lattice fringes and FFT peaks throughout the particle, indicating that our particles are made of small crystalline grains instead of amorphous phases.
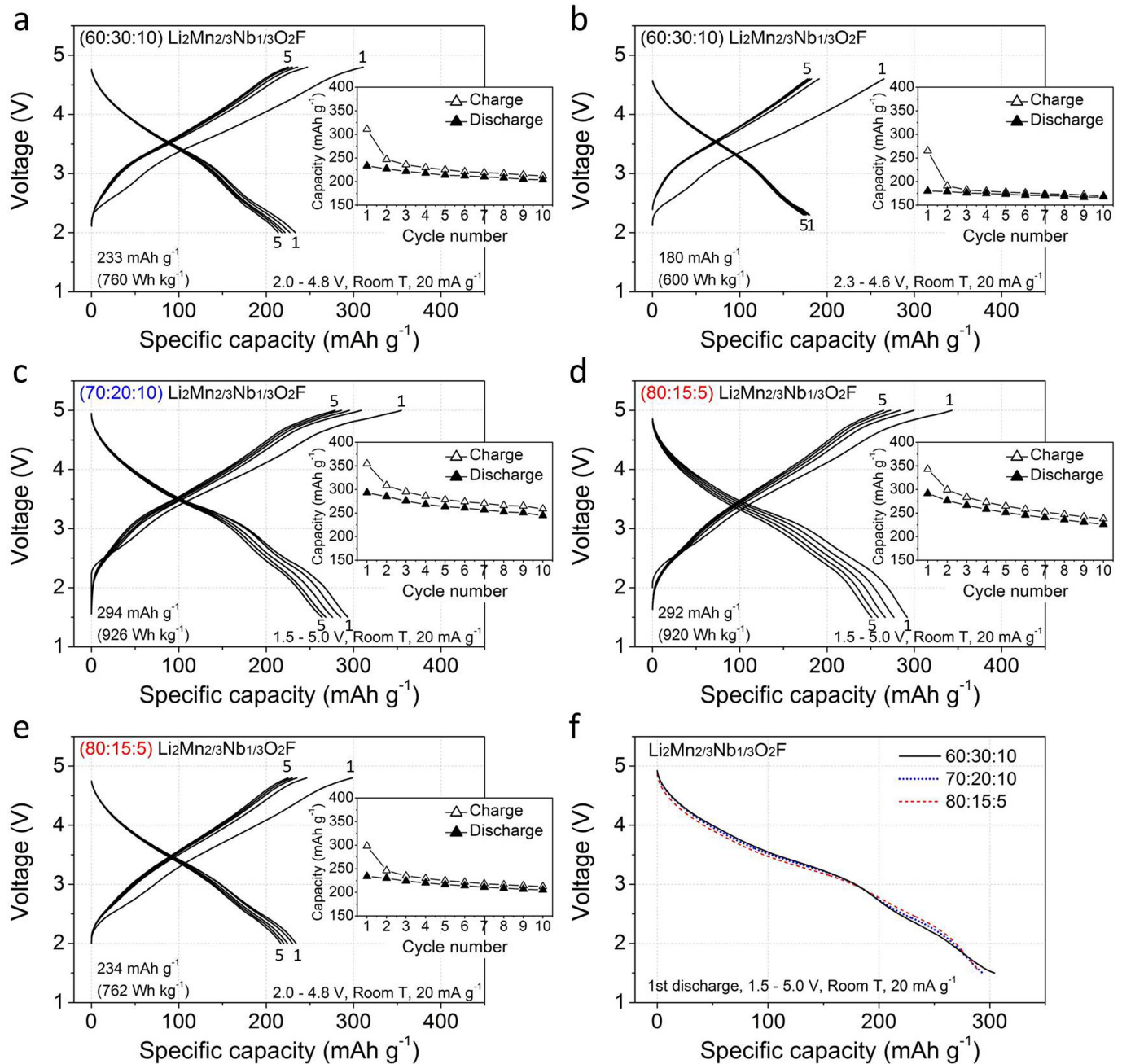
Extended Data Fig. 3 | Additional electrochemical data from Li₂Mn₂/₃Nb₁/₃O₂F. a, b, Voltage profiles of the 60:30:10 electrode (that is, 60 wt% Li₂Mn₂/₃Nb₁/₃O₂F: 30 wt% carbon black: 10 wt% PTFE) when cycled between 2.0 V and 4.8 V (**a**), and 2.3 V and 4.6 V (**b**) at 20 mA g⁻¹. **c, d,** Voltage profiles of the 70:20:10 (**c**) and the 80:15:5 (**d**) electrodes, when cycled between 1.5 V and 5.0 V at 20 mA g⁻¹. **e,** Voltage profiles of the 80:15:5 electrode when cycled between 2.0 V and 4.8 V at 20 mA g⁻¹. **f,** A comparison of the first discharge profiles of the 60:30:10, 70:20:10 and 80:15:5 Li₂Mn₂/₃Nb₁/₃O₂F electrodes (1.5–5.0 V, 20 mA g⁻¹). The specific capacity was calculated on the amount of the Li₂Mn₂/₃Nb₁/₃O₂F powder in the cathode film.
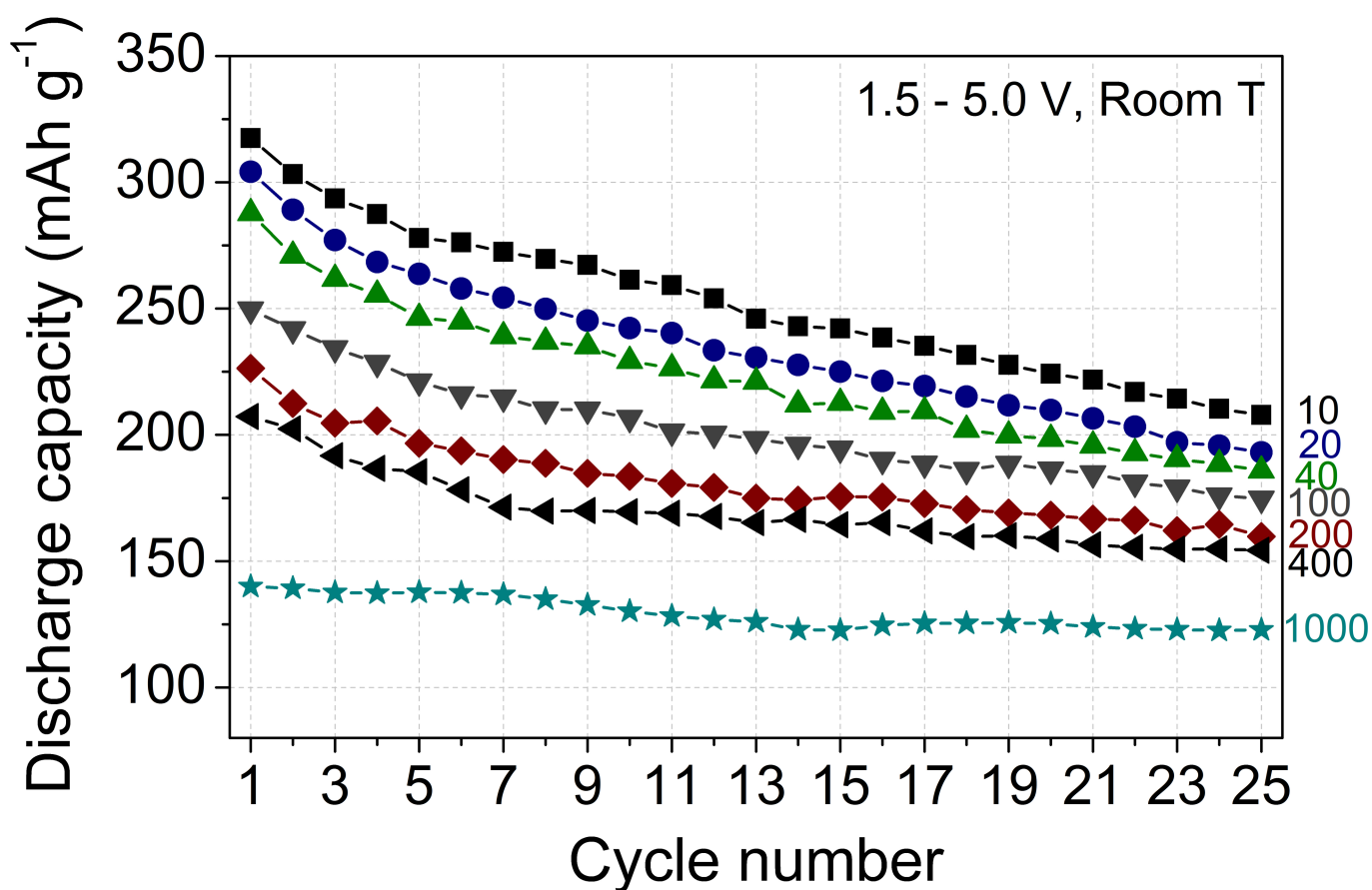
**Extended Data Fig. 4 | Discharge capacity retention.** The 60:30:10 $Li_2Mn_{2/3}Nb_{1/3}O_2F$: carbon black:PTFE electrode was cycled between 1.5 V and 5.0 V at room temperature at 10, 20, 40, 100, 200, 400 and 1,000 mA g^{-1}. A faster rate leads to less capacity fading during the initial 25 cycles. This is likely to be due to electrolyte decomposition per cycle occurring more (less) at a high voltage in a slower (faster) cycling test, which increases the impedance of a cell by creating a resistive surface layer and decreasing the ionic conductivity of the electrolyte.
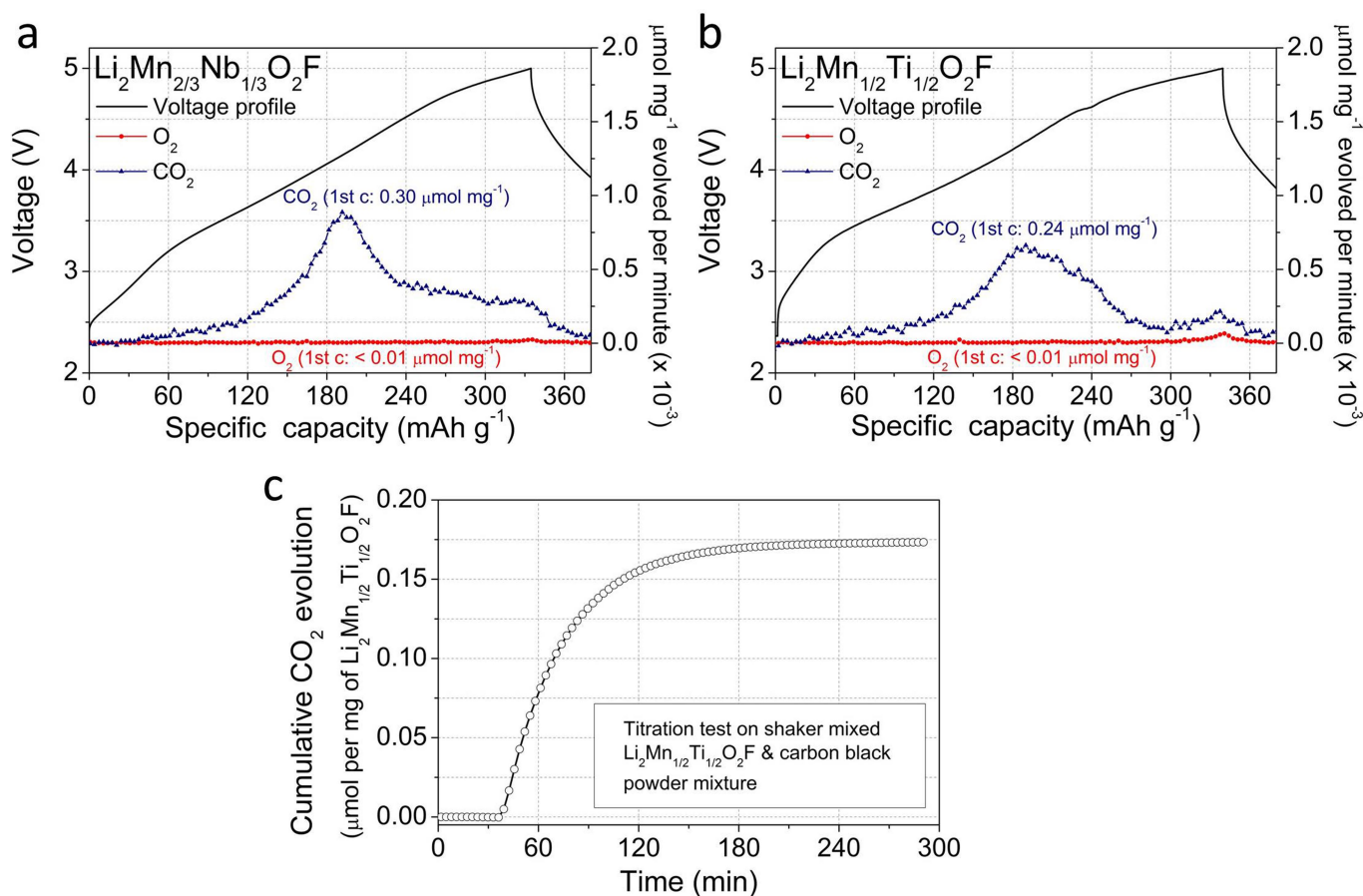
Extended Data Fig. 5 | Gas evolution measurements. a, b, Initial voltage profiles (black solid line) of $Li_2Mn_{2/3}Nb_{1/3}O_2F$ (**a**) and $Li_2Mn_{1/2}Ti_{1/2}O_2F$ (**b**), when charged to 5.0 V at a rate of 20 mA g^{-1}. DEMS results for O_2 (red circles) and CO_2 (blue triangles) evolution are also shown. **c,** Cumulative CO_2 evolution from shaker-mixed $Li_2Mn_{1/2}Ti_{1/2}O_2F$ and carbon black powder mixture, as a function of time during an acid titration test using 1 M H_2SO_4. Detailed explanations of the results are given in Methods section 'Supplementary Note 2'. 1st c, first charge.
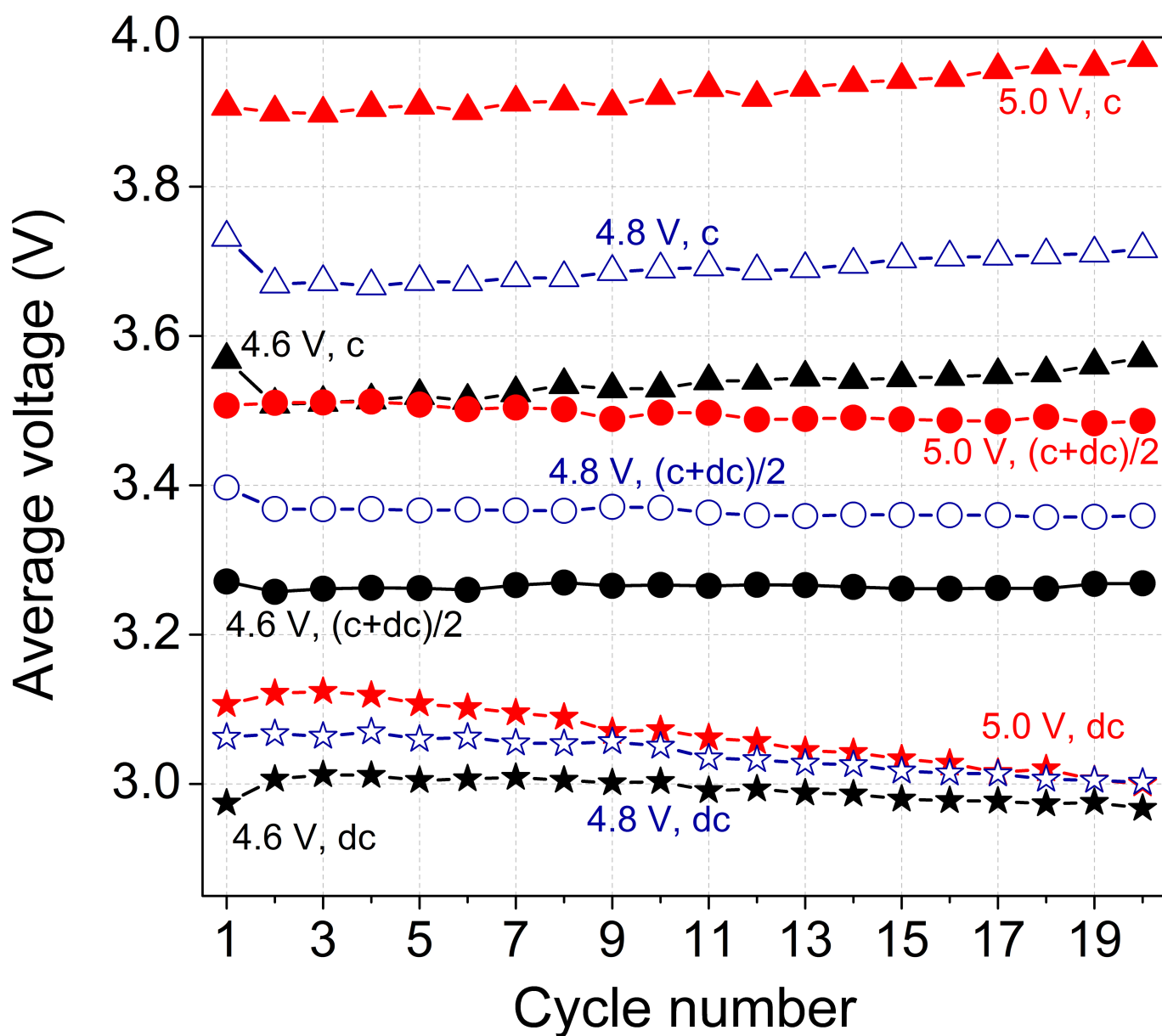
Extended Data Fig. 6 | Evolution of the charge and discharge voltages. Average charge voltage (triangles), discharge voltage (stars), and half of the charge–discharge voltage (circles) are shown when $Li_2Mn_{2/3}Nb_{1/3}O_2F$ is cycled between 1.5 V and 4.6 V, 1.5 V and 4.8 V, and 1.5 V and 5.0 V, at 20 mA g^{-1}. Detailed explanations of the results are given in Methods section 'Supplementary Note 3'. c, charge; dc, discharge.
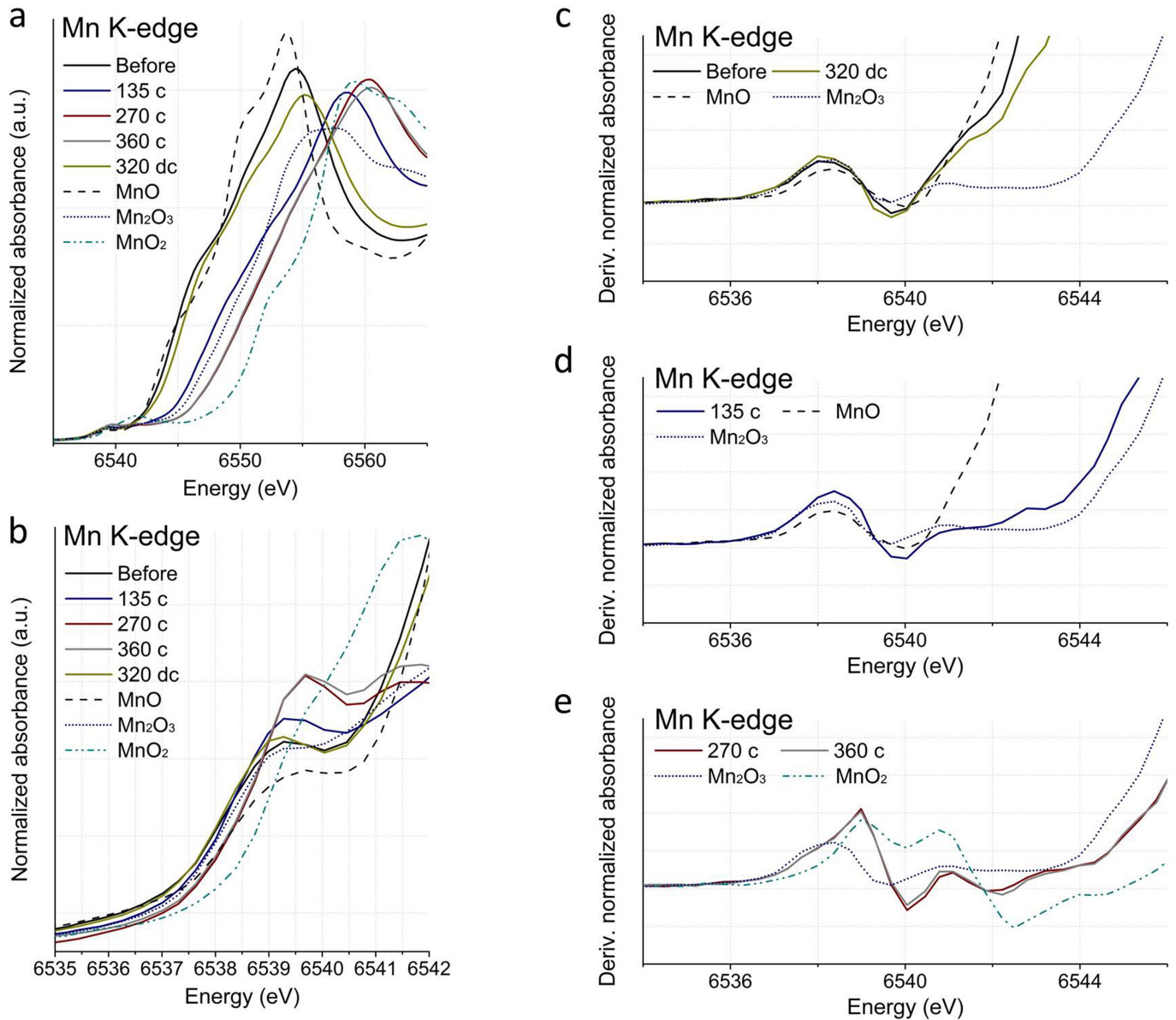
Extended Data Fig. 7 | XANES of Li$_2$Mn$_{2/3}$Nb$_{1/3}$O$_2$F. a, b, Manganese K-edge XANES spectra of Li$_2$Mn$_{2/3}$Nb$_{1/3}$O$_2$F: before cycle, after first charging to 135 mAh g^{-1}, 270 mAh g^{-1} and 360 mAh g^{-1}, and after first charging to 375 mAh g^{-1} then discharging to 320 mAh g^{-1}. **c–e**, First derivatives of normalized absorbance at the pre-edge region of Mn K-edge spectra of Li$_2$Mn$_{2/3}$Nb$_{1/3}$O$_2$F: **c**, before cycle and after first charging to 375 mAh g^{-1} then discharging to 320 mAh g^{-1}; **d**, after first charging to 135 mAh g^{-1}; and **e**, to 270 mAh g^{-1} and 360 mAh g^{-1}. Data from MnO, Mn$_2$O$_3$ and MnO$_2$ are presented for comparison. Detailed explanations of the results are given in Methods section 'Supplementary Note 4'.
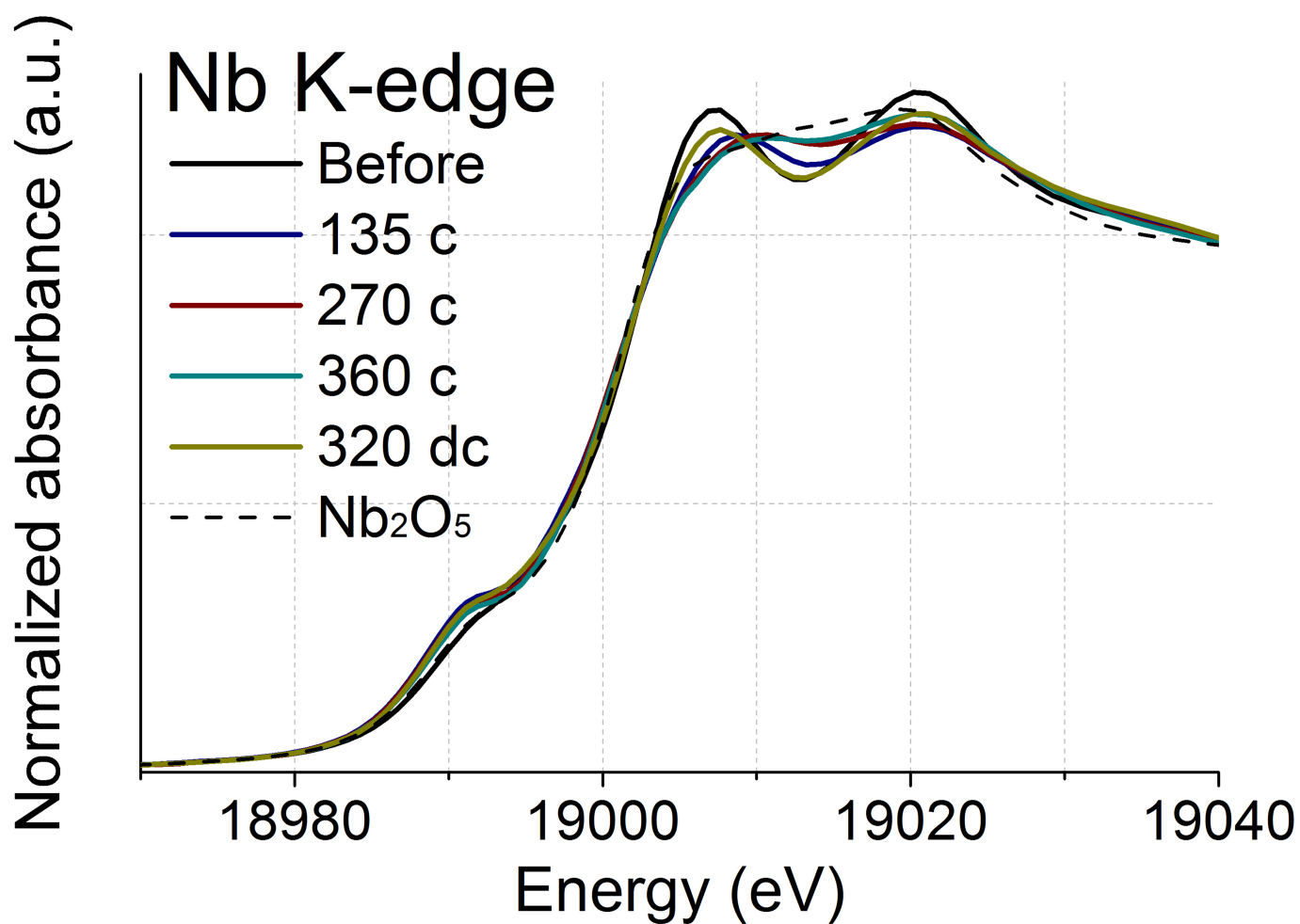
Extended Data Fig. 8 | Niobium K-edge XANES spectra of Li₂Mn₂/₃Nb₁/₃O₂F obtained by hard XAS. Results are shown before cycle, after charging to 135 mAh g⁻¹, 270 mAh g⁻¹ and 360 mAh g⁻¹, and after charging to 375 mAh g⁻¹ then discharging to 320 mAh g⁻¹. The Nb K-edge XANES spectra of the $Li_2Mn_{2/3}Nb_{1/3}O_2F$ samples are similar to that of Nb_2O_5 (Nb^{5+} reference), indicating that Nb in the compound stays as Nb^{5+} during cycling. The observable small shape changes are likely to be related to changes in local disorder and distortion[60].

a

c

1.1Å (400)
1.3Å (311), (222)
1.6Å (220)
2.1Å (200)

e

b

① ② ③ ④

d

① ② ③ ④
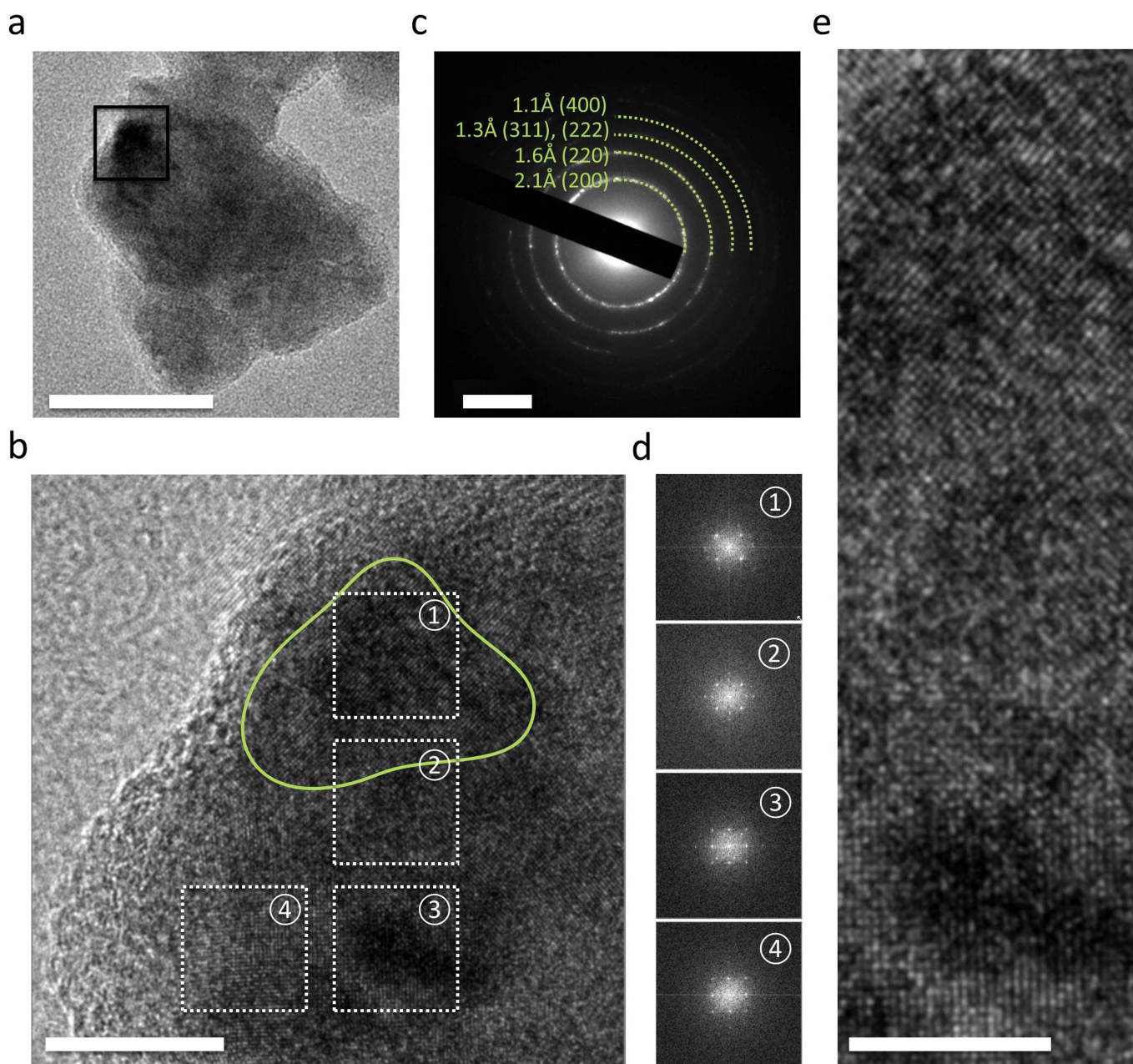
Extended Data Fig. 9 | Structural characterization of Li$_2$Mn$_{1/2}$Ti$_{1/2}$O$_2$F.
a, TEM image of as-synthesized Li$_2$Mn$_{1/2}$Ti$_{1/2}$O$_2$F particles. Scale bar, 50 nm. **b**, A high-magnification TEM image of the area enclosed in a square in **a**. Scale bar, 10 nm. The yellow circle indicates the boundary of one of the many grains in the polycrystalline Li$_2$Mn$_{1/2}$Ti$_{1/2}$O$_2$F particle. **c**, An electron diffraction pattern of the Li$_2$Mn$_{1/2}$Ti$_{1/2}$O$_2$F particle.

Scale bar, 5 nm^{-1}. **d**, FFT images of the dotted squared areas in **b**. **e**, The high magnification image across the squared areas 1, 2 and 3 in **b**. Scale bar, 5 nm. We can clearly observe lattice fringes and FFT peaks throughout the particle, indicating that our particles are made of small crystalline grains instead of amorphous phases.
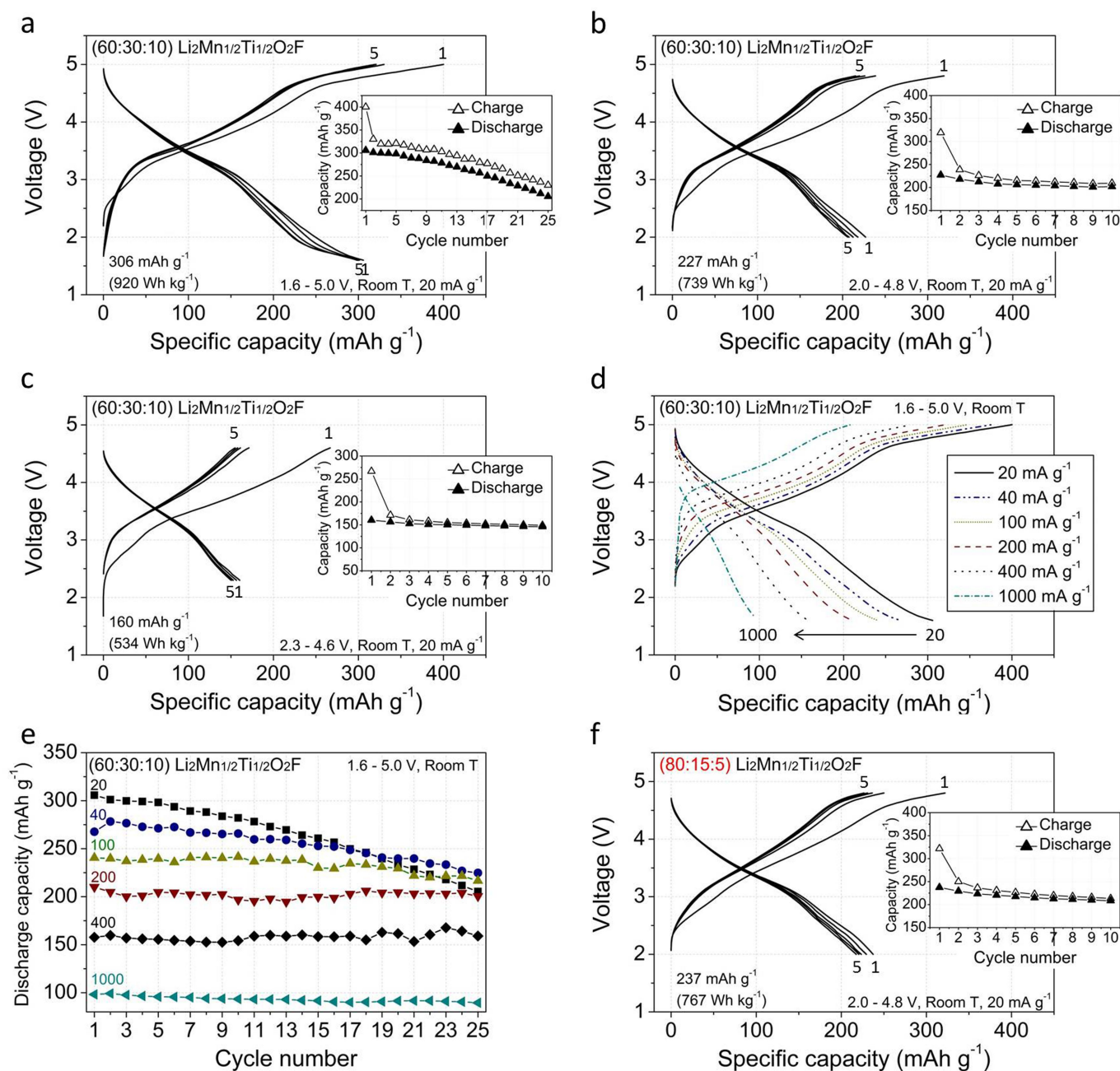
Extended Data Fig. 10 | Electrochemical properties of $Li_2Mn_{1/2}Ti_{1/2}O_2F$.
a–c, Voltage profiles and capacity retention of the 60:30:10
$Li_2Mn_{1/2}Ti_{1/2}O_2F$:carbon black:PTFE electrode when cycled at 20 mA g^{-1}
at room temperature between 1.6 V and 5.0 V (**a**), 2.0 V and 4.8 V (**b**), and
2.3 V and 4.6 V (**c**). **d**, The initial charge–discharge profile of the 60:30:10
electrode when cycled between 1.6 V and 5.0 V at room temperature at

20, 40, 100, 200, 400 and 1,000 mA g^{-1}. **e**, The discharge capacities during
initial 25 cycles. **f**, Voltage profiles and capacity retention of the 80:15:5
electrode when cycled at 20 mA g^{-1} at room temperature between 2.0 V
and 4.8 V. The specific capacity was calculated on the amount of the
$Li_2Mn_{1/2}Ti_{1/2}O_2F$ powder in the cathode film. Detailed explanations of the
results are given in Methods section 'Supplementary Note 5'.
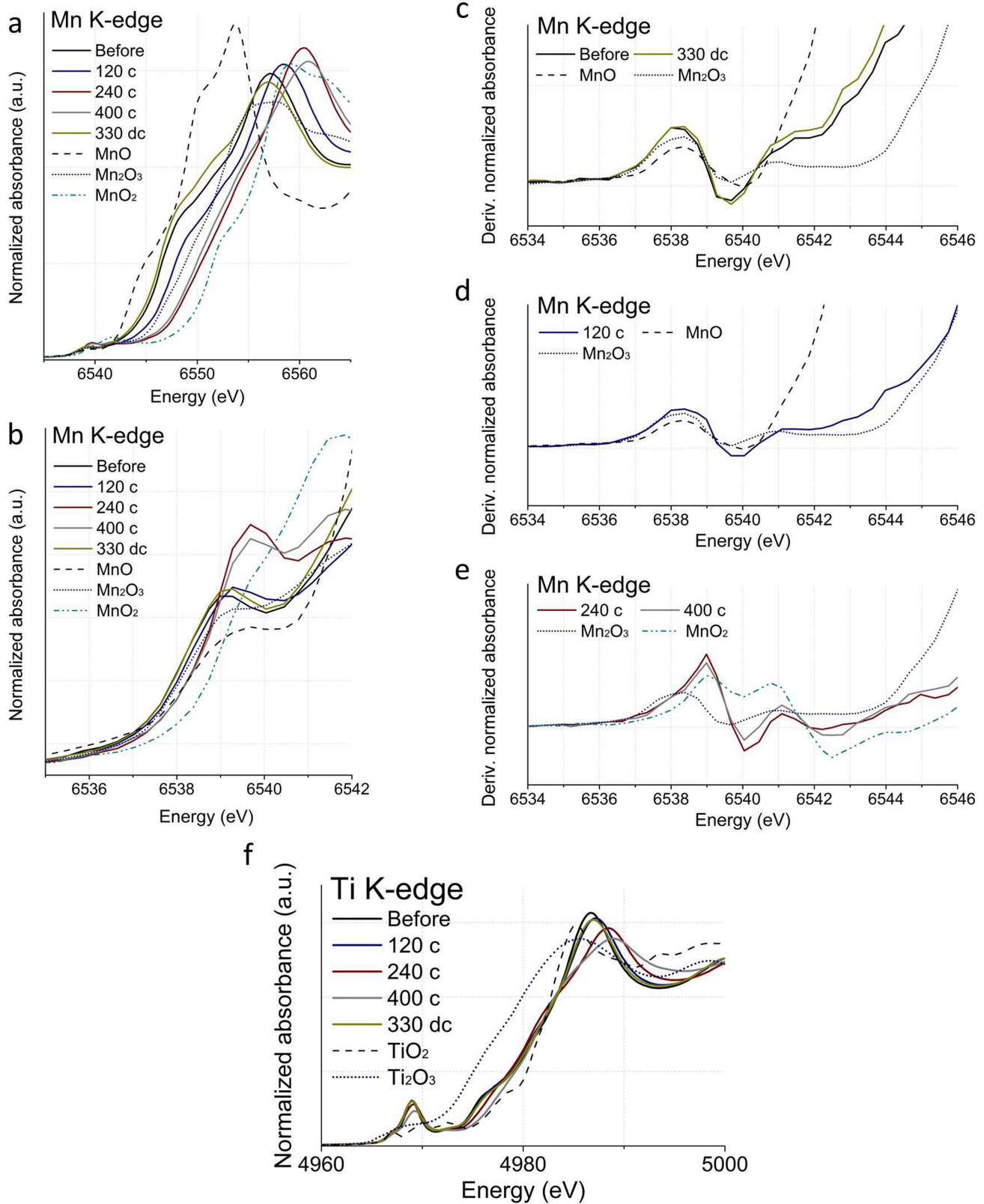
Extended Data Fig. 11 | XANES of Li₂Mn₁/₂Ti₁/₂O₂F. a, b, Manganese K-edge XANES spectra of $Li_2Mn_{1/2}Ti_{1/2}O_2F$: before cycle (black), 120 mAh g^{-1} charged (navy), 240 mAh g^{-1} charged (wine), 400 mAh g^{-1} charged (grey), 330 mAh g^{-1} discharged after a 400 mAh g^{-1} charge (dark yellow). **c–e**, First derivatives of normalized absorbance at the pre-edge region of Mn K-edge spectra of $Li_2Mn_{1/2}Ti_{1/2}O_2F$: **c**, before cycle and after

first charging to 400 mAh g^{-1} then discharging to 330 mAh g^{-1}; **d**, after first charging to 120 mAh g^{-1}; and **e**, to 240 mAh g^{-1} and 400 mAh g^{-1}. **f**, Titanium K-edge XANES spectra of $Li_2Mn_{1/2}Ti_{1/2}O_2F$ during the initial cycle. Data from MnO, Mn₂O₃, MnO₂, Ti₂O₃ and TiO₂ are presented for comparison. Detailed explanations of the results are given in Methods section 'Supplementary Note 6'.

Extended Data Table 1 | Structural parameters from the Rietveld refinements

Materials		$Li_2Mn_{2/3}Nb_{1/3}O_2F$	$Li_2Mn_{1/2}Ti_{1/2}O_2F$
Space group		Fm-3m	
R_{wp}		1.0023	1.1908
Goodness of Fit		0.7585	0.7494
B overall		0.1814 ± 0.0341	1.0236 ± 0.0297
Site 4a $(x, y, z) = (0, 0, 0)$	Li occupancy	0.6010 ± 0.0134	0.6537 ± 0.0135
	Mn occupancy	0.2244 ± 0.0033	0.1818 ± 0.0059
	Ti occupancy	0	0.1651 ± 0.0059
	Nb occupancy	0.1136 ± 0.0033	0
Site 4b $(x, y, z) = (0.5, 0.5, 0.5)$	O occupancy	0.6721 ± 0.0328	0.6442 ± 0.0384
	F occupancy	0.3279 ± 0.0328	0.3558 ± 0.0384
a (Å)		4.2615 ± 0.0008	4.2064 ± 0.0006
Volume (Å^3)		77.39	74.43
Derived density (kg/l)		3.78	3.52

The Rietveld refinements are shown in Figs. 1b and 5a. The crystallographic information file of $Fm\overline{3}m$ $LiFeO_2$ (ICSD collection code 51208) was used as an input file. A pseudo-Voigt fit was used ($U,V,W = 8.0691, -0.9697, 1.3778$ for $Li_2Mn_{2/3}Nb_{1/3}O_2F$, and $5.8736, -1, 1.4118$ for $Li_2Mn_{1/2}Ti_{1/2}O_2F$). The atomic occupancies were initially set to the atomic ratio obtained from elemental analysis by direct-current plasma emission spectroscopy and an ion-selective electrode, based on which the lattice parameters were first refined. We then further refined the lattice parameters and the atomic occupancies together. Transition-metal occupancies were first refined freely. Then O and F occupancies were individually refined with a constraint of their occupancies summing to 1. Finally, all atomic occupancies including Li occupancy were simultaneously refined with the additional constraint that the total transition-metal occupancy should stay unchanged during this final process. However, as O and F are difficult to distinguish by XRD, and Li cannot be seen clearly, their occupancy values are more subject to error.

Extended Data Table 2 | Target versus measured atomic ratio of $Li_2Mn_{2/3}Nb_{1/3}O_2F$ and $Li_2Mn_{1/2}Ti_{1/2}O_2F$ compounds

Materials	$Li_2Mn_{2/3}Nb_{1/3}O_2F$ (Li : Mn : Nb : F)	$Li_2Mn_{1/2}Ti_{1/2}O_2F$ (Li : Mn : Ti : F)
Target atomic ratio	2 : 0.666 : 0.333 : 1	2 : 0.5 : 0.5 : 1
Measured atomic ratio	1.852 : 0.660 : 0.333 : 1.05	2.01 : 0.514 : 0.475 : 1.05

Measurements were made by direct-current plasma emission spectroscopy (Li, Mn, Nb, Ti) and with an ion-selective electrode (F).